J. Fluid Mech. (1996), vol. 328, pp. 313–344

Turbulent structure beneath surface gravity waves sheared by the wind

By L. THAIS † AND J. MAGNAUDET
Institut de Mécanique des Fluides de Toulouse, UMR CNRS 5502,
2 Avenue Camille Soula, 31400 Toulouse, France

(Received 24 May 1995 and in revised form 9 July 1996)

New experiments have been carried out in a large laboratory channel to explore the structure of turbulent motion in the water layer beneath surface gravity waves. These experiments involve pure wind waves as well as wind-ruffled mechanically generated waves. A submersible two-component LDV system has been used to obtain the three components of the instantaneous velocity field along the vertical direction at a single fetch of 26 m. The displacement of the free surface has been determined simultaneously at the same downstream location by means of wave gauges. For both types of waves, suitable separation techniques have been used to split the total fluctuating motion into an orbital contribution (i.e. a motion induced by the displacement of the surface) and a turbulent contribution. Based on these experimental results, the present paper focuses on the structure of the water turbulence. The most prominent feature revealed by the two sets of experiments is the enhancement of both the turbulent kinetic energy and its dissipation rate with respect to values found near solid walls. Spectral analysis provides clear indications that wave–turbulence interactions greatly affect energy transfers over a significant frequency range by imposing a constant timescale related to the wave-induced strain. For mechanical waves we discuss several turbulent statistics and their modulation with respect to the wave phase, showing that the turbulence we observed was deeply affected at both large and small scales by the wave motion. An analysis of the phase variability of the bursting suggests that there is a direct interaction between the waves and the underlying turbulence, mainly at the wave crests. Turbulence budgets show that production essentially takes place in the wavy region of the flow, i.e. above the wave troughs. These results are finally used to address the nature of the basic mechanisms governing wave–turbulence interactions.

1. Introduction

The turbulent layer below a wavy free surface is one where turbulence can interact with a strongly energetic organized or random motion forced by an external agent, namely the displacement of the free surface. While the interactions between a wave field and a non-uniform mean current have been the subject of much theoretical and experimental work, wave–turbulence interactions have received comparatively little attention. Although it is more difficult to formulate the wave–turbulence interaction problem, there is a major fundamental interest in its investigation. This interest originates from the fact that turbulence and surface waves are two very different kinds

---

† Present address: School of Mathematics, University of Bristol, Bristol, BS8 1TW, UK.

of motions. One is basically three-dimensional and rotational (and thus dissipative) while the other is often, at least at large scales, nearly two-dimensional and potential (and thus conservative). There are also clear practical interests in the understanding of such interactions since turbulence near the free surface governs or at least influences many processes like gas and heat transfer across the interface, mixing in the upper layer of the oceans, prediction of wave growth rates, etc. Dealing with wave prediction for example, Belcher, Harris & Street (1994) showed that the wave growth rate was reduced by a factor of 2 when the turbulence in the water was accounted for in their analytical model of wave generation by the wind stress.

The primary motivation for the work reported in the present paper arises from the basic question: Can significant wave–turbulence interactions appear below a wavy free surface? This question can also be formulated concretely in the form: Does the turbulent structure in the top layer of water at a wavy air–water interface scale with laws valid for wall-bounded flows? Laboratory investigations reporting primary turbulence statistics usually give a positive answer to the latter question (Lin & Gad-el-Hak 1984; Terray & Bliven 1985; Yoshikawa et *al.* 1988; the wind-wave experiments of Cheung & Street 1988, hereinafter referred to as CS; and our own experiments, Magnaudet & Thais 1995, hereinafter referred to as I). In all these investigations the levels of the non-dimensional root-mean-squared (r.m.s.) turbulent velocities are found to be similar to those observed near rigid walls, leading to the provisional conclusion that random wind waves have no discernable effect on turbulence, even in the presence of significant wave breaking under strong wind conditions. To our knowledge, the only exception to this conclusion is the part of CS's experimental study devoted to the turbulent statistics beneath mechanically generated waves ruffled by light winds. In these experiments, CS noticed a significant enhancement of the non-dimensional r.m.s. turbulent velocities with respect to levels observed in a wall layer and with respect to all previous laboratory studies using pure wind waves.

The obvious constraining factor in laboratory channels is the limited fetch. Within these studies the fetch is always on the order of 10 m. While the turbulent layer is fully developed at a fetch of this order, the wave field is obviously not. The direct consequence of using large mechanically generated two-dimensional waves, as CS did, is to artificially increase the fetch and thus the wave energy for a given wind. Hence, the second question that naturally comes to mind is whether the fetch is the only relevant parameter affecting turbulence dynamics and any possible wave–turbulence interactions, or if the structure of the wave field, random or periodic, needs also be considered.

Field studies avoid the problem of a limited fetch. Unfortunately, comprehensive field measurements in the topmost layer of water are quite scarce. First there is the difficulty of making accurate and non-perturbing measurements. Secondly the rapid variability in both the direction and the intensity of the wind can complicate interpretation of field data. Finally there is the difficulty of identifying the real turbulent velocity because of the superposed random movement induced by the surface displacement (Kitaigorodskii & Lumley 1983). The last of these problems is also encountered in laboratory experiments but is more difficult to solve in the field. The wave-related motion in the top layer of the ocean is usually several orders of magnitude larger than the turbulent movement, whereas the order of magnitude of both motions is closer in usual laboratory experiments. This is why most field studies usually do not identify the turbulent kinetic energy but rather estimate its dissipation rate, ϵ_T, from velocity spectra. Notwithstanding, significant discrepancies appear amongst available ϵ_T estimates (see Terray *et al.* 1996, for a thorough review). While some studies show general agreement between ϵ_T and the wall scaling (e.g. Dillon *et al.* 1981; Jones 1985), others show substantial differences. For example, Kitaigorodskii *et al.* (1983) performed field measurements on Lake Ontario from a fixed tower. They used a linear separation of wave-induced and turbulent motions (Benilov, Kouznetzov & Panin 1974) and found that both the turbulent kinetic energy and its dissipation rate were dramatically increased with respect to usual shear flows. Using new data collected on the same site, Agrawal *et al.* (1992) found that ϵ_T was higher than the wall scaling by 2 orders of magnitude. Gargett (1989) reported analogous behaviours at sea.

Thus evidence exists showing that turbulence below wind waves does and does not obey wall scalings. Those who believe that turbulence is enhanced below deep water waves usually consider wave breaking responsible for production of the turbulence beyond shear-driven turbulence. While such a statement clearly applies in strong seas, where conspicuous intermittency of the sea state pleads in this direction, it is not yet clear whether it applies under gentle wind conditions. The ambiguity of the term ‘breaking’ was emphasized in the review of Banner & Peregrine (1993). In addition to large breakers the significance of small-scale breakers having amplitudes of a couple of cm has been realized at sea. Recently Longuet-Higgins (1992) provided evidence that a capillary breaker can generate high vorticity near the crest of larger gravity waves. Opposed to theories of wave breaking, in fact yet to be built (Banner & Peregrine 1993), stand theories of wave–turbulence interactions involving coupling between the mean current, the wave motion, and the turbulence (Magnaudet & Masbernat 1990). One goal of this study is to determine whether the former theories can hold under gentle wind conditions.

Moreover, while efforts have focused on global energetics and dissipation, little attention has been devoted to understand the energetic events that take place below a wavy free surface. To address the basic issues raised above, and given the possible influence of scaling, most notably the relative sizes of orbital and turbulent motions, it would seem helpful to make highly controlled laboratory experiments with wave scales that are closer to those formed in the field. Such experiments, performed in the large Air-Sea Interactions Facility of the ‘Institut de Mécanique Statistique de la Turbulence’ in Marseille are the subject of the present paper. The experimental device and signal processing techniques are presented in §2. Next §3 and §4 emphasize the effects of strong wave–turbulence interactions on the turbulent field: §3 deals with the global energetics of the turbulence while §4 examines its spectral properties. As we discuss in §5, when the waves are periodic the dynamics of the turbulent field can be analysed in detail. This section deals with the modulation properties of the turbulence and the characteristics of the bursting events below such waves. Finally, the problem of the nature and occurrence of wave–turbulence interactions is addressed in §6.

2. Experiments and signal processing

2.1. *Experimental conditions and measurements*

The experiments were conducted in the large Air-Sea Interactions Facility of the ‘Institut de Mécanique Statistique de la Turbulence’ (now IRPHE-IOA) in Marseille. Both wind waves and mechanical waves can be generated in this facility described by Coantic *et al.* (1981). The dimensions of the test channel are: 40 m long, 2.6 m high, 3.2 m wide. The measurements described below were made at a single downstream position (fetch) of nearly 26 m at fixed elevation, i.e. varying submergence beneath the wavy interface. During all the experiments the water depth H was set to 90 cm so that the waves considered here are deep water ones (the largest wavelength being about 1.6 m implies $kH \approx 3.6$, k denoting the peak wavenumber of the wave field). At the downstream end of the channel is a dissipative beach with a reflection coefficient lower than 8% for the waves generated in the present work.

Two series of experiments were carried out:

E1: pure wind waves (air free-stream velocities $U_\infty = 4.5\ \mathrm{m\,s^{-1}}$, $5.9\ \mathrm{m\,s^{-1}}$, and $7.8\ \mathrm{m\,s^{-1}}$)

E2: periodic waves ruffled by a light wind (air free-stream velocities $3.0\ \mathrm{m\,s^{-1}}$, $4.5\ \mathrm{m\,s^{-1}}$, and $5.8\ \mathrm{m\,s^{-1}}$ an additional experiment with no wind being used as reference).

During experiments E2 a piston-type wavemaker located at the upstream end of the channel was used to generate two-dimensional periodic surface waves having a frequency $f_0 = 1/T_0 = 1.0$ Hz and an amplitude $a = 27.0$ mm (wave slope $ak = 0.106$, where k is the wavenumber).

The experiments consisted of measuring the wave field at two nearby locations aligned on the centreline of the channel and the water velocity in the three space directions along the vertical axis situated at the same fetch as one of the wave gauges. In the following u, v and w denote the velocity components along the streamwise (x), spanwise (y) and vertical (z) axes, respectively, z being directed upwards and its origin, $z = 0$, taken at the mean water level. The wave height, denoted η, is measured with respect to the mean water level. The time evolution of η was recorded with the aid of capacitance-type gauges. The water velocity was simultaneously measured with a Doppler velocimeter operating in back-scatter mode. A full description of the optical and traversing systems, probe support mechanism, etc., can be found in I or in Thais (1994). Here emphasis is put on the improvements made with respect to I. These improvements mainly concern the velocity field measurements.

The laser beams were transmitted with a submerged 2-component optical fibre system DANTEC 60X17 using the blue and green lines of a 5 W Ar-Ion laser SPECTRA PHYSICS 167, whereas a one-component fibre was used in I. Positioning of the submerged laser head along the vertical direction, z, was performed with a high-precision electronically driven traverse system. The precision on the probe positioning is ± 0.05 mm. The upper limit of the measuring elevation was chosen as close as possible to the wave troughs to avoid interception of the laser beams by the free surface. For experiments E2 the smallest distance between the troughs of the large periodic wave and the upper position of the probe volume measure is between 2 and 4 mm (depending on the wind speed). Careful tests showing that no discernable disturbance is introduced in the flow by the submerged laser head have already been reported in I. The Doppler signals recorded over periods of 512 s were processed with two DANTEC 57N10 Burst Spectrum Analysers, BSA, whereas one frequency tracker was used in I. The irregularly sampled velocity signals issued by both BSA were stored with the aid of a first personal computer (PC1). Simultaneously, the two wave height signals were regularly acquired at a constant rate 200 Hz on a second computer (PC2) physically synchronized with PC1. The originally irregularly sampled water velocity was later resampled at the same constant rate (200 Hz) as the regularly sampled wave height. Resampling was performed with the reconstruction algorithm documented in Veynante & Candel (1988). This method was found more

U_∞ (m s^{-1})	f_0 (Hz)	c (m s^{-1})	$(\overline{\eta^2})^{1/2}$ (mm)	$\lambda = 2\pi/k$ (cm)	u_* (mm s^{-1})	U_l (cm s^{-1})
Wind Waves (E1)						
4.5	2.3	0.85	6.0	29.8	7.0	11.1
5.9	2.0	0.95	9.1	37.2	8.9	15.1
7.8	1.8	1.0	13.0	45.6	13.0	20.6
Mechanical Waves (E2)						
0.0	1.0	1.69	18.8	169	0.0	1.6
3.0	1.0	1.75	19.5	169	4.5	7.9
4.5	1.0	1.64	19.8	154	6.0	11.2
5.8	1.0	1.59	21.2	145	8.2	15.6

TABLE 1. Experimental conditions and characteristic scales. U_∞, air free-stream velocity; f_0, peak wave frequency; c, celerity of the peak wave; $(\overline{\eta^2})^{1/2}$, root mean square of the wave elevation; λ, peak wave length; u_*, water friction velocity; U_l, Lagrangian surface drift.

accurate than linear interpolation or 'sample-and-hold' algorithms. Careful tests of the reconstruction algorithm were performed on simulated LDV data to check for aliasing and statistical invariance with respect to the original irregular data (for further details, see Thais 1994).

In addition to wave height and water velocity measurements, the mean streamwise air velocity profile was determined with a Pitot static tube. The surface shear velocity in the air, u_{*a}, was inferred from the logarithmic part of this velocity profile, assuming a von Kármán constant $\kappa = 0.4$. As pointed out in §3.2 water turbulence statistics reported in the present paper are normalized with the friction velocity in the water, u_*. We calculate u_* from the matching of the shear stresses at the mean water level, i.e.

$$\rho_w u_*^2 = \rho_a u_{*a}^2 \tag{2.1}$$

where ρ_w and ρ_a are the water and air densities, respectively. Assumptions leading to (2.1) are discussed in §3.2.1.

The Lagrangian surface drift U_l was also determined by recording the time necessary for paper punchings to travel a known distance ($\approx$ 2.5 m) delineated by two strings and averaging the results over 20 realizations.

Table 1 summarizes the characteristic scales for the complete set of experiments.

2.2. *Wave–turbulence decomposition*

Over the last 20 years there has been a continuous refinement of the various methods available for deriving the velocity field beneath random waves from a single-point measurement of the surface elevation (see Thais & Magnaudet 1995, hereinafter referred to as II). Most of these methods find their motivation in engineering problems such as calculation of wave forces on coastal or off-shore structures. Our objective in the present work is quite different since it lies in the extraction of the turbulent component superimposed on the wave motion when the wind blows. Much of the earlier work was based on the linear model of a random sea (see Donelan, Anctil & Doering 1992 for an excellent review), i.e. the waves were assumed potential and linearly superposed.

In this work we used two different separation schemes described below according to the nature of the wave field (pure wind waves or mechanically generated ruffled waves). Since the wave field was only characterized by single-point measurements, no information was available on the angular spreading of the waves with respect to the direction of the wind. Thus both separation methods are two-dimensional, i.e. no separation was performed on the spanwise fluctuation v. However, in the context of pure wind waves (most likely more three-dimensional than mechanical waves), it was shown in I that in a range of wind speeds comparable to those of the present experiments only a few percent of the r.m.s. of v were due to the orbital motion.

2.2.1. *Wind waves (E1)*

In II it was emphasized that it is incorrect to consider the wave-related motion as purely potential when wind waves travel on a mean sheared current. It was demonstrated in I that wind waves generated in short-fetch laboratory channels strongly disturb the vorticity associated with the mean drift and that substantial wave-related vorticity exists. More precisely, near the surface the rotational part of the orbital motion was found to contain nearly 20% of the total r.m.s. orbital velocity. As a consequence, linear techniques assuming a potential behaviour of the orbital motion are clearly inadequate for such waves. This is the reason why our data from experiments E1 have been processed using the nonlinear triple decomposition method (TDM) thoroughly described in II and summarized here. Basically the fluctuating water velocity $\boldsymbol{v}$ is split into three contributions

$$\boldsymbol{v} = \tilde{\boldsymbol{v}}_P + \tilde{\boldsymbol{v}}_R + \boldsymbol{v}', \tag{2.2}$$

where $\tilde{\boldsymbol{v}}_P$ and $\tilde{\boldsymbol{v}}_R$ are the potential and rotational wave-related components and $\boldsymbol{v}'$ is the remaining turbulent contribution. The first stage of the TDM consists of computing the time evolution of $\tilde{\boldsymbol{v}}_P$ by means of a least-square optimization algorithm solving both the nonlinear kinematic and dynamic boundary conditions written on the real free surface (Jiang, Street & Klotz 1990). The second stage consists of subtracting $\tilde{\boldsymbol{v}}_P$ from $\boldsymbol{v}$ and correlating the realization $\boldsymbol{v} - \tilde{\boldsymbol{v}}_P$ with the wave elevation so as to extract the spectral features of $\tilde{\boldsymbol{v}}_R$ and $\boldsymbol{v}'$. The key hypothesis of the TDM is that all the wave components travel at the unique phase speed c of the spectral peak (non-dispersive behaviour), which means that each wave component is frozen in the frame of reference moving at speed c. Experimental results (Ramamonjiarisoa 1974) and theory (Lake & Yuen 1978) support this behaviour for wind waves generated in laboratory channels, especially under strong wind conditions. Phillips (1981) attributes this property to the enhanced short-crestedness of waves generated in wind tunnels and subsequent destruction by breaking of the free-wave components. Careful tests were carried out in II and showed that the velocity field beneath laboratory wind waves is accurately predicted using this assumption.

2.2.2. *Mechanical waves (E2)*

Blowing a light wind over a two-dimensional periodic wave field (with wave period T_0) causes the growth of a turbulent layer in the water. This physical situation is intuitively different from pure wind waves. For periodic waves the most natural decomposition scheme of the water velocity happens to be a phase averaging identifying the long-wave component,

$$\langle \boldsymbol{v} \rangle = \frac{1}{N_W} \sum_{n=0}^{N_W-1} \boldsymbol{v}(t + nT_0), \tag{2.3}$$

where N_W is the number of available wave groups with wave period T_0. This technique has many advantages. In particular it does not assume linearity or potential

U_∞(m s^{-1})	0.0	3.0	4.5	5.8
E_{sw}	0.1	2.5	3.7	8.4

TABLE 2. Energy carried by the short waves, $E_{sw} = 100(\hat{\eta}_{sw}/\overline{\eta^2})$, in experiments E2 for various air free-stream velocities U_∞.

behaviour for the wave-related motion. The 'turbulent' velocity field $\boldsymbol{v}_T$ is defined as the non-periodic part of the velocity, namely

$$\boldsymbol{v}_T = \boldsymbol{v} - \langle \boldsymbol{v} \rangle. \tag{2.4}$$

Phase averaging is not as straightforward as it would seem. The difficult point is to achieve an accurate computation of the wave period T_0 because (2.3) involves a large number of waves ($N_W \approx 512$) for the sake of statistical convergence. Any error of the order of the sampling period $T_S = 1/200$ s would propagate through one wave period over 200 waves, each having a frequency of approximately 1 Hz. To avoid this pitfall the following strategy was adopted. A first guess for T_0 was computed by counting the zero-crossings of η with positive slope. An iterative procedure was then used with the first guess as initial value. The iterative scheme proceeded until the amplitude a of the phase average of η was found to be a maximum. Tests with simulated data demonstrated that the final precision for the wave period is of order $\pm 4.10^{-5}$ s.

Unfortunately, if the mechanical wave is initially two-dimensional and periodic, the wind generates short random waves riding over the longer one. Thus η is actually the sum of the periodic wave elevation $\langle \eta \rangle$ and the short-wave component, say η_{sw},

$$\eta = \langle \eta \rangle + \eta_{sw}. \tag{2.5}$$

Then, the total wave-related velocity is the sum of the periodic component and of the component induced by the short waves $\tilde{\boldsymbol{v}}_{sw}$, i.e.

$$\tilde{\boldsymbol{v}} = \langle \boldsymbol{v} \rangle + \tilde{\boldsymbol{v}}_{sw}, \tag{2.6}$$

whereas the 'real' turbulent velocity field is written

$$\boldsymbol{v}' = \boldsymbol{v}_T - \tilde{\boldsymbol{v}}_{sw}. \tag{2.7}$$

To check whether or not it is important to account for the energy carried by the short waves at the measuring fetch, the phase average $\langle \eta \rangle$ of the wave elevation was subtracted out of the total wave elevation. The variance of the short waves was computed through $\hat{\eta}_{sw} = \overline{(\eta - \langle \eta \rangle)^2}$, where the overbar stands for time averaging.

Table 2 shows $\hat{\eta}_{sw}/\overline{\eta^2}$ as a function of the wind speed. It can be seen that η_{sw} contains up to 8% of the total energy of the wave field. Such levels imply that a simple phase average is insufficient to identify properly the turbulent velocity field. This point has already been singled out by CS, even though they found that not much energy was carried by the short waves owing probably to the shorter fetch in their experiments. CS overcame the problem with a linear spectral estimate of the r.m.s. velocity $(\overline{\tilde{u}_{sw}^2})^{1/2}$ induced by the short waves. They subtracted $\overline{\tilde{u}_{sw}^2}$ from $\overline{u_T^2}$ and $\overline{w_T^2}$, which were their turbulent variances estimated, as a first approximation, from phase averaging (equation (2.4) above). This technique has the serious drawback of acting on the mean-square statistical quantities; as a consequence, the time history of the turbulent signal $\boldsymbol{v}'(t)$ remains unknown.

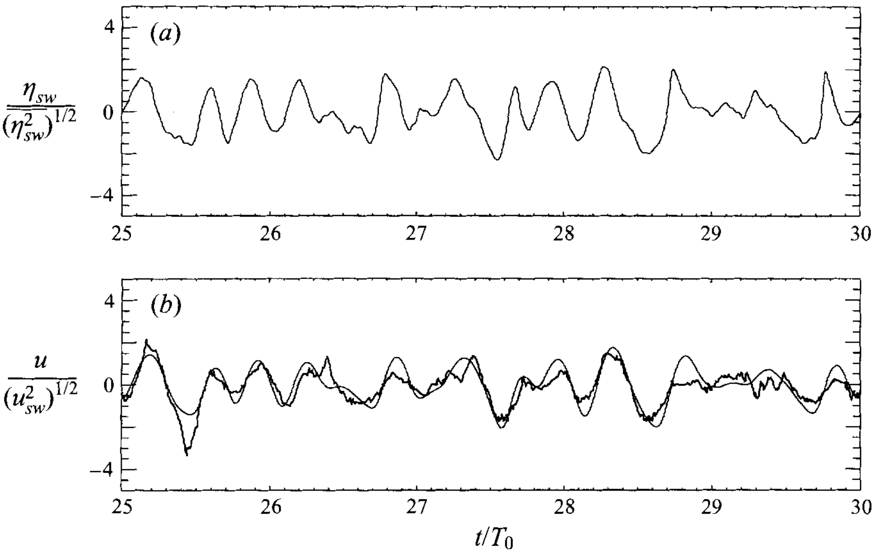

FIGURE 1. Illustration of the linear superposition technique (LST); (a) ripples $\eta_{sw} = \eta - \langle \eta \rangle$ (b) ——, u_{sw} computed with η_{sw}; ——, $u - \langle u \rangle$.

When considering the objective of computing the time evolution of $\boldsymbol{v}'(t)$, the TDM is not more suitable than phase averaging. The main reason for this is that the non-dispersive hypothesis is inappropriate for experiments E2 owing to the relative weakness of the wind energy input with respect to the energy carried by the dominant wave. Indeed, the nonlinear model of wind waves developed by Lake & Yuen (1978) does not apply for ripples overriding a long linear wave.

An alternative is to compute the time evolution of $\tilde{\boldsymbol{v}}_{sw}(t)$ from $\eta_{sw}(t)$ with the linear superposition technique (LST) developed by Donelan *et al.* (1992). This technique is appropriate for linear random waves each propagating at its own phase speed given by the linear dispersion relation. In brief, the method consists of Fourier transforming the wave height $\eta_{sw} = \sum_{n=1}^{N} a_n \exp[\mathrm{j}(k_n x - \omega_n t + \theta_n)]$ and assuming that the wave motion derives from the deep water velocity potential

$$\Phi_{sw} = \sum_{n=1}^{N} \mathrm{j}\frac{a_n g}{\omega_n} \exp(k_n z) \exp[\mathrm{j}(k_n x - \omega_n t + \theta_n)], \tag{2.8}$$

where $\mathrm{j} = \sqrt{-1}$ and the radian frequency is $\omega_n = (g k_n)^{1/2}$. The potential Φ is reconstructed by successively adding shorter wave components. Rather than applying directly the LST to η, we first compute the phase average of η and apply the method to the short-wave elevation η_{sw}. The reason for this is that since $\langle \eta \rangle$ is by far the dominant contribution to the surface elevation (it actually contains the wave at frequency $1/T_0$ and its bound harmonics), nearly all the nonlinear and rotational contributions in the orbital motion lie in $\langle \boldsymbol{v} \rangle$. For example features like a possible phase lag between $\langle u \rangle$ and $\langle w \rangle$, which are likely to be prominent at the dominant wave frequency, are captured within the phase average. The efficiency of the overall method is illustrated in figure 1 where typical samples of η_{sw}, $\tilde{u}_{sw}$, and $u - \langle u \rangle$ are plotted. The difference $u - \langle u \rangle$ includes of course $\tilde{u}_{sw}$ as well as the turbulent velocity component u' due to the wind stress. It is clear that $u - \langle u \rangle$ and $\tilde{u}_{sw}$ are highly correlated proving that:

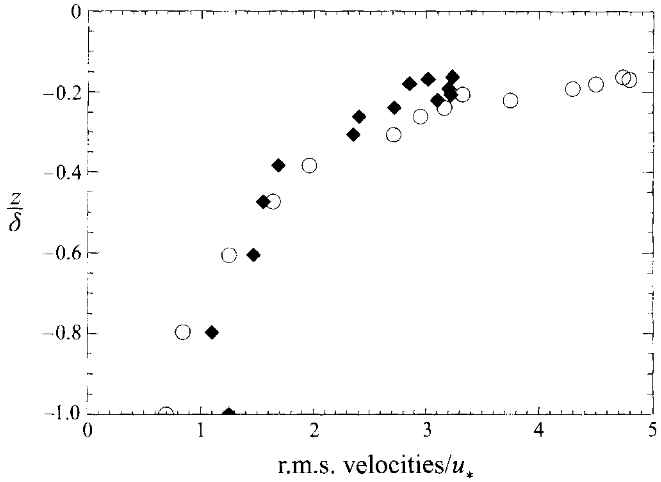

FIGURE 2. Vertical profile of: ◆, the streamwise turbulent velocity $(\overline{u'^2})^{1/2}/u_*$; and ○, the ripples component $(\overline{\tilde{u}^2_{sw}})^{1/2}/u_*$ (experiments E2, $U_\infty = 4.5$ m s^{-1}).

(*a*) the LST, as applied in the present work, is efficient for computing the dynamics of the short waves overriding the long waves;

(*b*) the velocity $\tilde{u}_{sw}$ has the same order of magnitude as the turbulence.

As a better illustration of this, figure 2 shows a vertical profile of $(\overline{\tilde{u}^2_{sw}})^{1/2}$ and $(\overline{u'^2})^{1/2}$ at the intermediate wind speed 4.5 m s^{-1}. The r.m.s. velocity $(\overline{\tilde{u}^2_{sw}})^{1/2}$ is larger than $(\overline{u'^2})^{1/2}$ close to the surface. Therefore it would be wrong to neglect $\tilde{u}_{sw}$ because the turbulent level near the surface would be overestimated by a factor as large as 2. Note that capillarity is not taken into account in (2.8). Capillary ripples must exist around the crest of the dominant wave (Longuet-Higgins 1963; Ebuchi, Kawamura & Toba 1987). Since our measurements are all located below the trough level the velocities directly induced by the capillaries are negligible, owing to their very rapid vertical decay.

3. Energetic properties of the three contributions to the fluctuating motion

3.1. *Wave-induced motion*

Globally speaking both the potential and the rotational contributions to the wave-induced motion exhibit features similar to those that we have already described in detail in I. For that reason we will just summarize here the main characteristics displayed by these motions in the present experiments. In agreement with our previous observations (see I) the vertical profiles of the potential wave-induced motion $(\overline{\tilde{u}^2_P})^{1/2}$ and $(\overline{\tilde{w}^2_P})^{1/2}$ (not shown here) collapse within a narrow band when scaled with appropriate velocity and length scales. The suitable velocity scale is the integrated surface orbital velocity $\tilde{u}_{PS} = \tilde{u}_{Pz}(0)$ deduced from the general expression (see I)

$$\tilde{u}_{Pz}(z) = 2\pi\,(1 - U_0/c)\left[\int f^2 S_\eta(f)\exp(4\pi f z/c)\,\mathrm{d}f\right]^{1/2}, \qquad (3.1)$$

where $S_\eta(f)$ is the power spectral density of the wave field, c the absolute phase velocity of the dominant wave and U_0 the Eulerian drift current at the mean surface level.

The appropriate length scale is the value of the depth z for which $\tilde{u}_{Pz}(z) = \mathrm{e}^{-1}\tilde{u}_{PS}$. It is the inverse of the peak wavenumber for mechanical wave experiments.

The profiles of the rotational wave-induced contributions $(\overline{\tilde{u}_R^2})^{1/2}$ and $(\overline{\tilde{w}_R^2})^{1/2}$ (not shown) have been found to be of significant magnitude in experiments E1 as in I. In experiments E2 the rotational contribution lies within $\langle \boldsymbol{v} \rangle$ and was not analysed separately. Near the surface, $(\overline{\tilde{u}_R^2})^{1/2}$ reaches 20% of $\tilde{u}_{PS}$, whereas $(\overline{\tilde{w}_R^2})^{1/2}$ is systematically half this level. Both profiles have quite different decays. As already discussed in I these trends prove that $(\overline{\tilde{u}_R^2})^{1/2}$ and $(\overline{\tilde{w}_R^2})^{1/2}$ characterize really a rotational motion and are not velocities associated with free waves which would be spuriously rejected by the first step of the separation method. The fact that the rotational contribution is found to be of significant magnitude confirms our primary conclusion in I: the wave-related motion cannot be regarded as purely potential in the case of active generation by the wind shear. The mechanisms able to generate a wave-related vorticity were discussed in I. The conclusion supported by our measurements was that, under laboratory conditions, the vertical inhomogeneity of the mean current acted to redistribute vorticity between the mean drift and the wave-related motion. This conclusion is likely to apply in the present experiments and since our goal is to focus this paper on turbulence we do not repeat the analysis here. Moreover the specific features displayed by the mean drift will be analysed in another paper (Monismith *et al.* 1996). The role played by the rotational wave-related motion in the wave–turbulence interaction mechanisms is addressed in §6.

3.2. *Second-order moments of the water turbulence*

3.2.1. *Determination of the water friction velocity, u_**

The appropriate velocity scale of the water turbulence is the water friction velocity, u_*, deduced from (2.1), expressing the tangential stress continuity at the surface. Expression (2.1) is based on the assumption that the entire momentum flux from the wind drives the turbulent flow in the water. In other words (2.1) assumes that the interface is in local equilibrium with the wind. CS determined u_* through a least-squares interpolation of $-\overline{u'w'}$ up to the mean water level. We find it preferable to use shear-stress continuity owing to the specific properties of the water turbulence to be described below. The interpolation of $-\overline{u'w'}$ in the water would lead to a small overestimate of u_*. In contrast no unexpected features were observed in the airflow, suggesting that the determination of u_* through the air mean velocity profile was suitable. Our results for the water friction velocity are indeed consistent with CS's values at equivalent wind speeds.

3.2.2. *Turbulence statistics*

Figure 3 depicts the vertical profiles of the dimensionless turbulent kinetic energy $\overline{k_t}u_*^2 = (\overline{u'^2} + \overline{v^2} + \overline{w'^2})/2u_*^2$ found in the present experiments. Also plotted for comparison are our data from I and the classical results of Klebanoff (1955) for a turbulent boundary layer. The depth has been made non-dimensional with the boundary layer thickness, δ, defined as the depth where the turbulent shear stess, $\overline{u'w'}$, cancels. Within each set of experiments the data collapse into a narrow band. Clearly the profiles corresponding to the present experiments E1 and E2 exhibit dramatic departures from those observed in wall boundary layers or below laboratory wind waves in experiments performed under shorter fetch conditions (see CS and I). For example in experiments E1 the maximum non-dimensional turbulent kinetic energy is of order 20, and of order 30 in experiments E2. These values are respectively 5 and

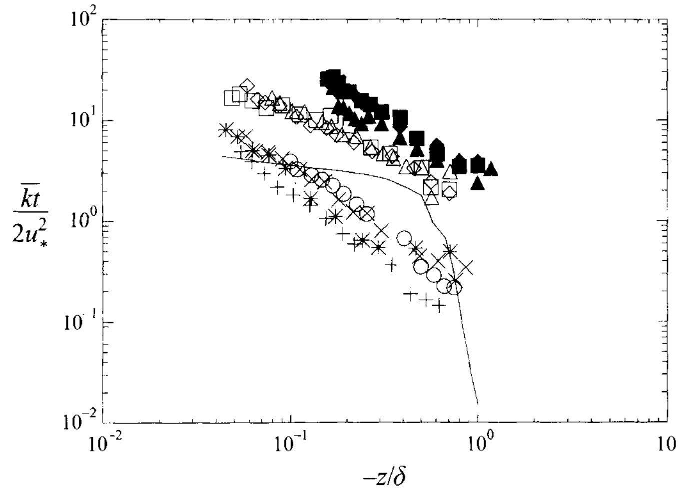

FIGURE 3. Non-dimensional kinetic energy: (*a*) experiments E2: ■, $U_\infty = 3.0$ m s^{-1}; ◆, $= 4.5$ m s^{-1}; ▲, $= 5.8$ m s^{-1}. (*b*) experiments E1: □, $U_\infty = 4.5$ m s^{-1}; ◇, $= 5.9$ m s^{-1}; △, $= 7.8$ m s^{-1}. (c) I: *, $U_\infty = 4.5$ m s^{-1}; ×, $= 6.8$ m s^{-1}; +, $= 9.0$ m s^{-1}; ○, $= 13.5$ m s^{-1}; ——, Klebanoff (1955).

7 times larger than the maximum turbulent kinetic energy found in usual boundary layers (Klebanoff 1955). With regard to decay laws of the turbulent kinetic energy with depth, a power-law fit of each series of experiments leads to a $z^{-1.0}$ decay for E2, a $z^{-0.9}$ decay for E1, while a $z^{-1.3}$ decay was found in I. A slight change of slope is noticed in the series corresponding to the strongest wind in I. This behaviour discussed in I is related to the three-dimensinal characteristics of laboratory wind waves under strong wind conditions. As shown by figure 3 all these decays are much more rapid than those observed in wall boundary layers (Klebanoff 1955).

In I and CS $(\overline{u'^2})^{1/2}$ and $(\overline{w'^2})^{1/2}$ reached maximum values of $2.5u_*$ and $1.5u_*$, respectively. Here similar quantities (not shown) reach maximum values of $3.3u_*$ and $3.4u_*$ respectively for experiments E1 and $3.8u_*$ and $4.0u_*$ respectively for experiments E2. These maximum values suggest considering the degree of isotropy, defined in the vertical plane (x,z) as

$$R_{iso} = \left(\overline{u'^2}/\overline{w'^2}\right)^{1/2}. \tag{3.2}$$

This ratio is found to be approximately constant along the vertical axis. Averaged along the vertical direction z, its mean value is $R_{iso} \approx 1.2$ for experiments E1, and $R_{iso} \approx 0.9$ for experiments E2, in contrast with 1.7 in a usual boundary layer.

It is worth pointing out that these unusual results also differ dramatically from those observed in turbulent layers over small-amplitude wavy terrain (Belcher, Newley & Hunt 1993) or over small-amplitude moving waves (Hsu, Hsu & Street 1981). The work by Hsu *et al.* is particularly relevant for comparison since they used small-amplitude waves almost identical to ours ($a = 26.7$ mm, $ak = 0.107$). Their experiments show that the perturbations to the air flow are within 10% of the total fluctuations. It has long been known that the air flow does not separate over small-amplitude waves. Belcher & Hunt (1993) showed how the perturbations to the air flow are predicted by a linear theory ascribing the small enhancement of turbulent statistics to a non-separated sheltering effect (to leading order). Recirculations occur only over large-amplitude undulations; see for example Buckles, Hanratty & Adrian (1984) in which flow past a sinusoidal wall with $ak = 0.64$ is studied. Our experimental

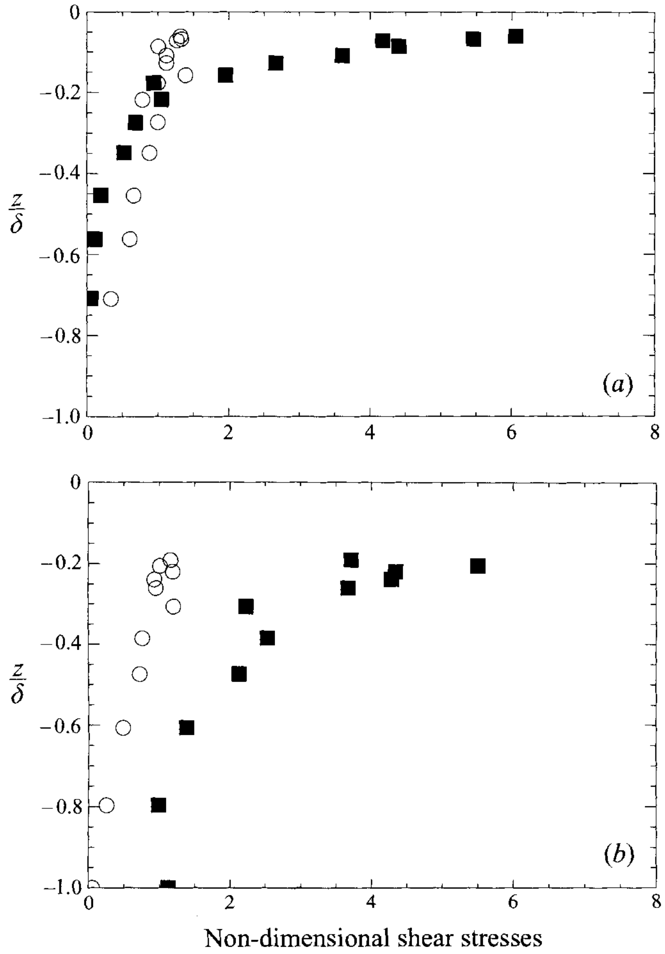

FIGURE 4. Non-dimensional shear stresses: ○, turbulent shear stress $-\overline{u'w'}/u_*^2$; ■, wave-related shear stress $-\overline{\tilde{u}\tilde{w}}/u_*^2$. (*a*) Experiments E1, $U_\infty = 5.9$ m s^{-1}; (*b*) experiments E2, $U_\infty = 4.5$ m s^{-1}.

conditions clearly do not match with such extreme slopes which anyway cannot be sustained by water waves.

Therefore, the present turbulence levels are substantially different from those found in usual flat-wall flows or over small-amplitude waves. In contrast, they are quite comparable to those observed on Lake Ontario by Kitaigorodskii *et al.* (1983). Impressively high levels of turbulence were observed below wind waves by these authors, typically $(\overline{u'^2})^{1/2} \approx (\overline{w'^2})^{1/2} \approx 8.0u_*$. Our results thus confirm that under certain conditions (to be discussed in §6) the level of turbulence can be dramatically increased underneath surface waves sheared by the wind.

Let us now examine the behaviour of the shear stresses. Since the orbital velocity field is not truly potential the shear stress includes a turbulent and a wave-induced contribution. Typical profiles of both the turbulent shear stress $-\overline{u'w'}$ and its wave-induced counterpart $-\overline{\tilde{u}\tilde{w}}$ taken from experiments E1 are plotted on figure 4(*a*). The turbulent shear stress is positive and decays almost linearly with depth. Extrapolating this profile up to the mean surface would lead to a non-dimensional surface value nearly equal to 1.3. However this extrapolation is highly questionable since crucial phenomena (see §6) take place in the wavy region above the troughs that are not described by our measurements. This was our basic motivation for using equation (2.1) to determine u_*. The wave-related shear stress is also positive and reaches $7.0u_*^2$ underneath the wave troughs. The penetration depth of $-\overline{\tilde{u}\tilde{w}}$ (defined as the depth at which the quantity reaches half of its surface value) is about half of the penetration depth of $-\overline{u'w'}$. These results are completely different from those of CS who found below wind-water waves negative wave-related shear stresses lower than u_*^2 with a penetration depth 5 times less than the penetration depth of $-\overline{u'w'}$. Our results indicate that the effects of wave-induced vorticity (the origin of $-\overline{\tilde{u}\tilde{w}}$, see I) extend over most of the turbulent boundary layer and are not confined to the immediate vicinity of the surface. The corresponding results for experiments E2 are plotted on figure 4(*b*). This figure shows trends qualitatively similar to those observed with wind waves. However, owing to the larger wavelength of the mechanical wave the wave-induced shear stress $-\overline{\tilde{u}\tilde{w}}$ decays more slowly and dominates the turbulent shear stress over the whole depth covered by the measurements.

3.3. *Dissipation rate*

Since the measurements reveal an unusually high turbulence level it is of primary interest to get an estimate of the dissipation rate. For that purpose, starting from frequency spectra, a suitable Taylor's hypothesis is required since turbulence is advected by a combination of the mean ($\bar{U}$) and orbital ($\tilde{u}_{P_z}$) motions. According to the model of Lumley & Terray (1983) which was derived for frozen homogeneous isotropic turbulence, assuming that $\tilde{u}_{P_z} \gg \bar{U}$, the dissipation can be estimated from the high-frequency equilibrium subrange of the spectra (far beyond the wave peak, $f \gg f_0$) through

$$\epsilon_T = \frac{4}{\tilde{u}_{P_z}} \left[\frac{110}{7\Gamma(1/3)C_K} S_{u'}(f) \right]^{3/2} (\pi f)^{5/2}, \tag{3.3}$$

where C_K, the Kolmogorov constant, is set to 1.5 and $S_{u'}(f)$ is the power spectral density of the turbulent velocity u'. Under the assumptions made by Lumley & Terray (1983) the power spectral densities of u' and w' are identical because the orbital motion is circular in the (x,z)-plane. Nevertheless, when possible, we estimated the dissipation rate using the high-frequency inertial subrange of the streamwise turbulent velocity spectra since it was generally better defined on this component. The dissipation rate normalized with the wall scaling $\epsilon_P = u_*^3/\kappa|z|$ is reported in figure 5 where it is apparent that ϵ_P is not an appropriate scaling factor for collapsing the data.

Our previous results from I and present experiments E1 show a large scatter but are largely in agreement with wall levels. One may note however a small enhancement in experiments E1 where ϵ_T is often twice the wall level in the upper layer. Things are clearer for experiments E2 where the dissipation rate is up to one order of magnitude larger than the wall level. Although these estimates contain a substantial amount of uncertainty, there is a clear connection between the turbulence energy level and its dissipation rate: the higher the turbulence level, the higher the dissipation. The 'usual' rates are recovered when the waves do not affect the turbulence level. Since the turbulent energy is mainly related to the low-frequency range of the spectra whereas the high-frequency range is used for estimating the dissipation, these results also give additional support to the separation methods used to split the velocity fluctuations into wave-induced and turbulent contributions: if the very high levels of turbulence reported above were simply the consequence of an inaccurate separation, the dissipation rates which involve only frequencies at least one order of magnitude higher than the typical wave frequency would keep their

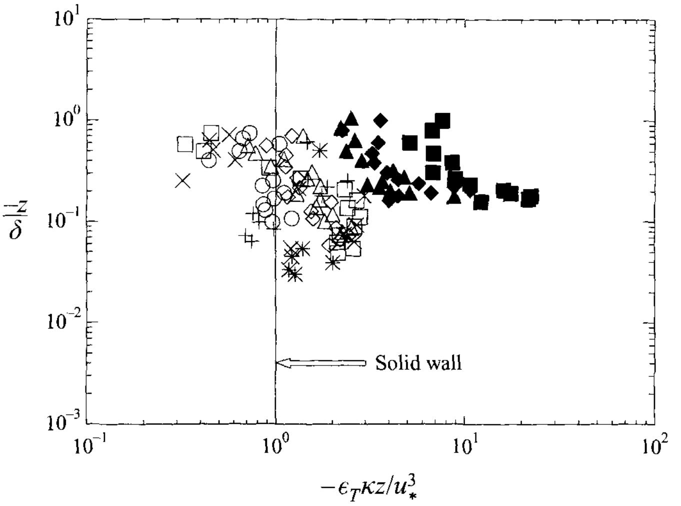

FIGURE 5. Non-dimensional dissipation rate; same symbols as figure 3.

usual values. To our knowledge, this work is the first to report such high dissipation rates below laboratory waves under relatively moderate wind conditions. However, this behaviour is in full agreement with several field measurements that have already found a dramatic enhancement of dissipation in the top of the water column either at sea (e.g. Gargett 1989), or in lakes (Kitaigorodskii *et al.* 1983; Agrawal *et al.* 1992). Trends similar to those displayed by ϵ_T in experiments E2 have also recently been observed in the absence of wind by Nepf *et al.* (1995) who studied breaking of mechanical waves in a laboratory channel.

4. Spectral characteristics

4.1. *Slopes and energy ratios*

A typical streamwise turbulent velocity spectrum from experiments E1 is shown in figure 6(*a*). This spectrum exhibits a substantial $f^{-5/3}$ decay on the frequency range [0.05, 1 Hz]. Another $f^{-5/3}$ region is observed at higher frequencies beyond 10 Hz (this is the subrange from which dissipation was deduced). As previously reported in I, a small bump is visible around the dominant wave frequency f_0 (here $f_0 = 2$ Hz), the origin of which was discussed in great detail by Lumley & Terray (1983). Nevertheless the most interesting feature is the occurrence of a f^{-3} decay in the frequency range [3, 10 Hz]. Also plotted on figure 6 is the power spectral density multiplied by f^3 to show the extent of the f^{-3} subrange. This remarkable feature was not present in I and there seems to be a close connection between its occurrence and the strong increase observed in both the turbulence energy level and its dissipation rate. The turbulence spectra from experiments E2 display the same trends, as shown in figure 6(*b*). A f^{-3} decay is again observed on the frequency range [3, 10 Hz].

Velocity spectra exhibiting a f^{-3} decay are usually typical of dynamics where the characteristic timescale is the same for all spatial scales. This situation can exist when external forces fix this timescale (e.g. the Coriolis force in geostrophic turbulence, Pedlosky 1987, the Lorentzian force in MHD turbulence, Sommeria & Moreau 1982). Thus the question that arises is whether the waves are able to impose on the turbulence a constant timescale over a significative spectral range. Since our measurements

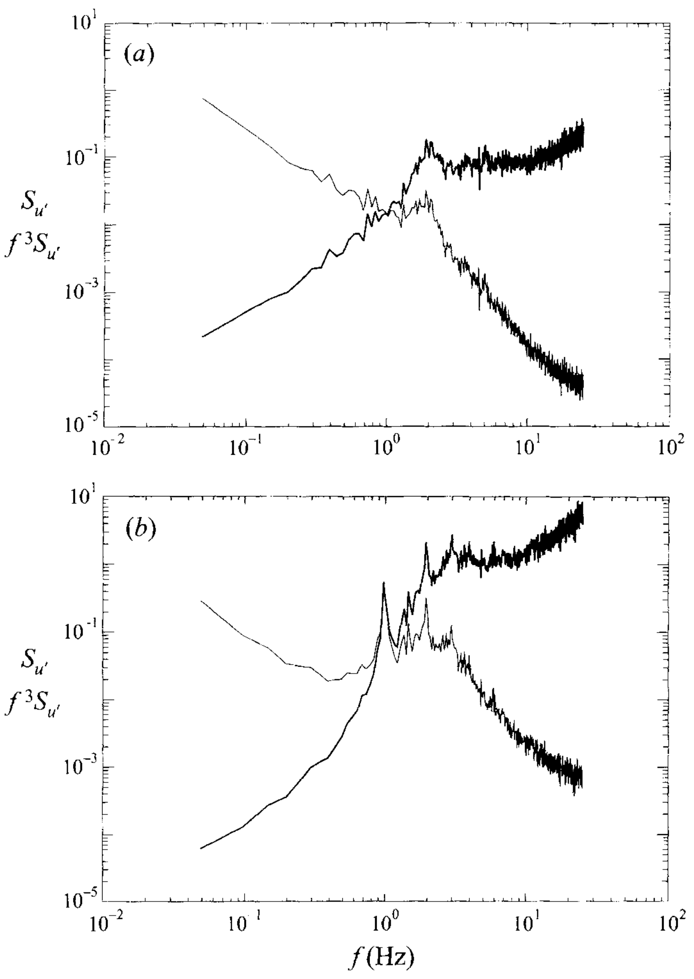

FIGURE 6. Typical spectra of the streamwise turbulent velocity: ——, power spectral density $S_{u'}$; ——, $f^3S_{u'}$. (*a*) Experiments E1, $U_\infty = 5.9$ m s^{-1}; (*b*) experiments E2, $U_\infty = 4.5$ m s^{-1}.

involve one-dimensional frequency spectra, this question cannot be answered without examining the kinematic processes that could alter the slope of the equilibrium range in frequency spectra with respect to the slope of the corresponding wavenumber spectra.

Two such processes can be identified. First, the slope might be distorted if no substantial mean velocity is available to bodily transport the turbulence. In this case, the usual Taylor hypothesis is invalid. However, the theoretical model of Lumley & Terray (1983) demonstrates that near the dominant wave frequency f_0, the kinematic effect of the orbital velocity field is to transform a usual $k^{-5/3}$ equilibrium subrange into two $f^{-5/3}$ subranges separated by a pronounced bump. The spectra computed by Lumley & Terray show that above the bump (i.e. $f \geqslant f_0$) the slope continuously decays from the maximum reached at $f = f_0$ to $-5/3$ without any tendency to produce an intermediate linear subrange. This is the behaviour exhibited in the results described in I. Thus it seems reasonable to conclude that this kinematic alteration cannot be the origin of the large f^{-3} range found in the present results.

The second possible process that could alter the slope of the frequency spectra is related to the properties of the wave field itself. Let us consider a random wave field with a saturation range as defined by Phillips (1977). Dimensional analysis shows that the wavenumber power spectral density $S_\eta(k)$ of such a wave field is commensurate with k^{-3}. If the waves are dispersive the wave frequency spectrum $S_\eta(f)$ should be commensurate with f^{-5}; if they are not dispersive it should be commensurate with f^{-3}. To leading order the orbital velocity spectrum is related to $S_\eta(f)$ through

$$S_{\tilde{u}}(f) = (2\pi f)^2 \mathrm{e}^{2kz} S_\eta(f). \tag{4.1}$$

As a consequence, near the surface $|2kz| \ll 1$, and $S_{\tilde{u}}$ decays as f^{-3} if the waves are dispersive and as f^{-1} if they are not. This behaviour means that if no separation is performed on the velocity signal it is possible to observe a f^{-3} subrange in the spectrum. For example, Revault d'Allonnes (1982) analysed spectra of the total velocity fluctuation and observed a f^{-3} subrange. In contrast, for experiments E1 we have filtered the wave-related motion $\tilde{u}$ out of the total velocity fluctuation with the TDM. This method assumes that the waves are not dispersive (see II) so that if this assumption were wrong a f^{-3} slope would be present somewhere. However, once the potential orbital motion has been filtered within the frame of the TDM, the remaining signal is correlated with the wave height η to extract the orbital rotational motion $\tilde{\boldsymbol{v}}_R$. Hence, if dispersive waves were badly computed in the first step of the TDM, their contribution would be projected onto the $\tilde{\boldsymbol{v}}_R$ spectra, but not onto the turbulent spectra. For experiments E2 the first step of the separation method (phase averaging) makes no assumption about the nature (dispersive or not) of the dominant wave while the second step explicitly takes into account dispersion. Thus we have to conclude that for both sets of experiments the f^{-3} decay observed in the turbulent spectra is really due to dynamics (i.e. it corresponds actually to a k^{-3} decay) and not to an artefact related to kinematics.

Let us turn back to the question raised above concerning the possible existence of a constant timescale. If waves act as a source of turbulence (through mechanisms to be discussed in §6), turbulence is forced by the orbital motion at least in a certain spectral range. Then in addition to the usual turbulent timescale $t_T = \epsilon_T^{-1/3} k^{-2/3}$, a second timescale t_W that is only related to wave properties becomes relevant. Dimensional arguments show that t_W is directly related to the inverse of the wave-induced strain rate $\partial \tilde{u}_i / \partial x_j$. In the case of a narrow wave spectrum centred around wavenumber k_0 we thus have

$$t_W(z) = (k_0 \tilde{u}_{Pz})^{-1}. \tag{4.2}$$

Obviously, at a given depth z, (4.2) represents a constant timescale which does not scale with any property of the turbulent motion. If turbulence dynamics is dominated by the wave motion over a significant range of wavenumber, then in this range the turbulent spectra will take the general form $S(k) \sim t_W^{-2} k^{-3}$. According to the analysis of Lumley & Terray (1983) this turbulence is advected by the orbital motion whose typical scale is $\tilde{u}_{Pz}$. Thus the corresponding frequency spectra must take the form

$$S(f) = C\, t_W^{-2}\, \tilde{u}_{Pz}^2\, f^{-3}. \tag{4.3}$$

In order to check whether or not t_W is really the timescale associated with the f^{-3} subrange present in our experimental spectra, the quantity $Q = S(f)\, t_W^2\, \tilde{u}_{Pz}^{-2} f^3$ was evaluated using both u' and w' spectra. According to (4.3) Q must be constant if our assumption is correct. The timescale t_W was computed by generalizing (4.2) to

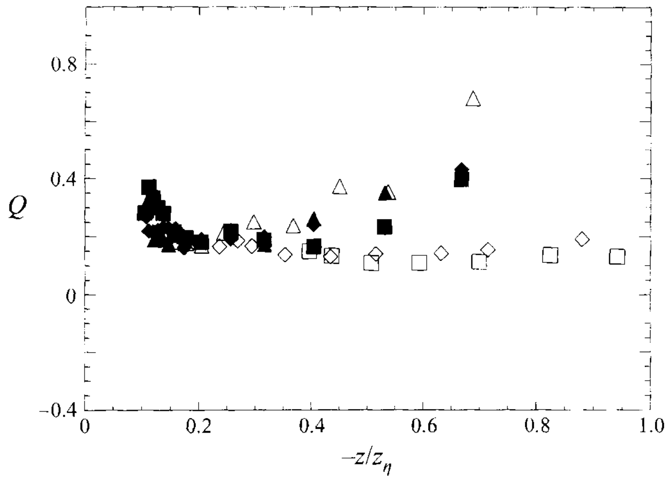

FIGURE 7. Test of the wave-strain scaling in the f^{-3} subrange of turbulence spectra (equation (4.3)); same symbols as figure 3.

spectra of finite width, namely

$$t_W^{-1} = 4\pi^2 c^{-1}\left(1 - U_0/c\right)\left[\int f^4 S_\eta(f)\exp\left(4\pi f z/c\right)\mathrm{d}f\right]^{1/2}. \qquad (4.4)$$

Figure 7 shows that, for $|z/z_\eta| \leqslant 0.5$, Q remains fairly constant, leading to $C \approx 0.2$ in equation (4.3). At larger distances the exponential decay of $\tilde{u}_{Pz}$ and t_W^{-1} introduces a considerable uncertainty and the results become unconsistent. Very near the trough level the increase of Q is probably due to the fact that equation (4.4) underestimates the local wave-related strain because rotational wave-induced velocities not included in (4.4) are important in this region. Bearing in mind that the uncertainty on Q can be estimated to 25% for $|z/z_\eta| \leqslant 0.5$, the result shown in figure 7 strongly supports the idea that in a certain range of scales, spectral transfers are governed by a constant timescale fixed by the wave-related strain. This leads us to conclude that the f^{-3} decay displayed by all the turbulent spectra obtained in the present experiments is indeed a manifestation of dynamic wave–turbulence interactions. In contrast if wave–turbulence interactions are not significant this behaviour must be absent. This is exactly what was observed in our earlier investigation I: the turbulent kinetic energy and its dissipation rate were found essentially in accordance with wall levels and no f^{-3} range appeared in the spectra. Based on spectral slopes, the idea that this f^{-3} decay may be connected in some way to a two-dimensonal behaviour of the turbulence in the vertical plane (x, z) has already been suggested by Lemmin, Scott & Czapski (1974), Donelan (1978) and Revault d'Allonnes (1982). In contrast with these investigations, we measured the spanwise velocity fluctuation v, a typical spectrum of which is shown in figure 8. No solution was found to extract properly $\tilde{v}$ from the total fluctuation v (see §2).This is why a pronounced spike is observed in this spectrum around the wave peak frequency. Even without separation it is clear from figure 8 that a turbulent fluctuation v' with an order of magnitude similar to that of u' and w' exists below the waves. Thus the turbulent field has indeed three components.

The spectral distribution of turbulence between the vertical and streamwise components is given by the ratio $R_S = S_{w'}(f)/S_{u'}(f)$. This ratio was computed on the

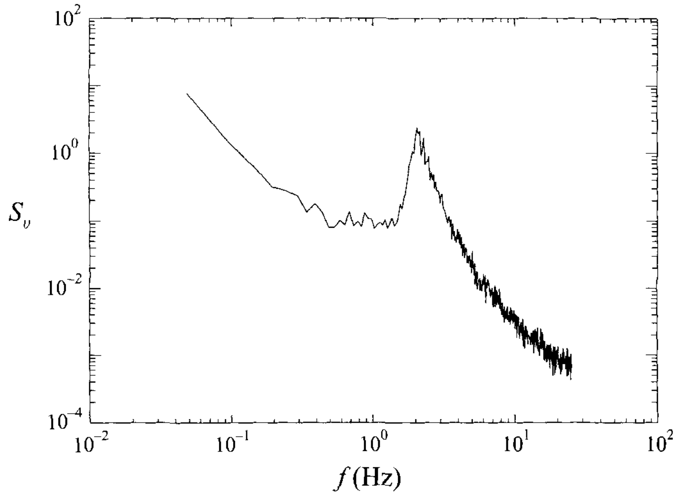

FIGURE 8. Typical spectrum of the spanwise velocity fluctuation close to the wave troughs (experiments E1, $U_\infty = 5.9\ \mathrm{m\,s^{-1}}$).

one hand in the low-frequency range $f \ll f_0$ and on the other hand in the f^{-3} range. These values were averaged over depth and over the whole set of experiments. In the low-frequency range we find $R_S \approx 1.2$ for experiments E1 and $R_S \approx 1.6$ for experiments E2. While in qualitative agreement with the theoretical value 4/3 corresponding to homogeneous three-dimensional isotropic turbulence it is clear that R_S is consistently larger in experiments E2. In light of the discussion above we note that R_S in that case is close to 5/3, the theoretical value for two-dimensional turbulence. In contrast the result obtained in the f^{-3} range is quite different. In both sets of experiments we find $R_S \approx 1$. As pointed out in §3.3 this result was obtained by Lumley & Terray (1983), assuming that turbulence was isotropic. It is a consequence of the fact that for $f > f_0$, turbulence is advected by the orbital velocities which act similarly and with the same magnitude along the vertical and streamwise directions. Thus, finding experimentally $R_S \approx 1$ is a good indication that, under our experimental conditions, turbulent scales corresponding to $f > f_0$ are very close to isotropy.

4.2. *Integral scales*

The integral timescale of the ith component of the motion is defined by the relation (Tennekes & Lumley 1972)

$$T_{v_i} = \frac{\pi S_{v_i}(0)}{\overline{v_i^2}}. \tag{4.5}$$

In the low-frequency range turbulence is advected along the streamwise direction. Consequently all three integral timescales defined by (4.5) only characterize the turbulent structure along this direction. Owing to the lack of wave–turbulence separation in the spanwise velocity component we have $\overline{v^2} = \overline{\tilde{v}^2} + \overline{v'^2} > \overline{v'^2}$, meaning that (4.5) is a lower bound for the integral scale of the spanwise fluctuation. Figure 9 depicts vertical profiles of T_u, T_v, and T_w for experiments E1. The uncertainty for these estimates of the integral scales is not negligible (typically ±25%) because of the extrapolation of the spectral density to zero frequency. However, it seems obvious that T_u and T_w are nearly equal whereas the transverse integral scale is always much larger. The latter trend increases towards the bottom of the channel

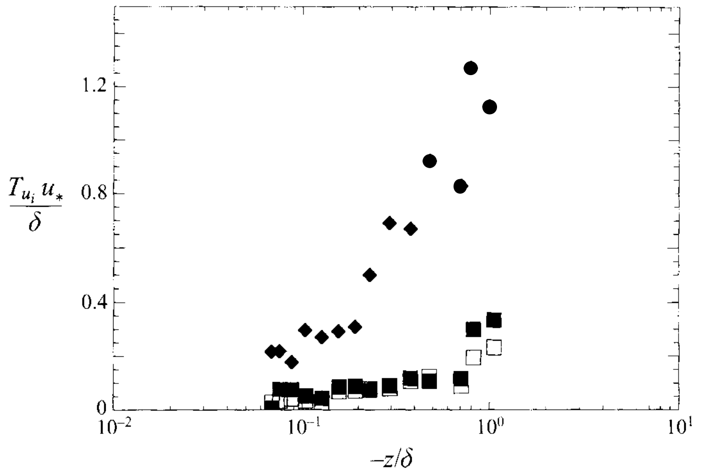

FIGURE 9. Integral timescales along the streamwise direction: ■, streamwise velocity T_u; □, vertical velocity T_w; ◆, spanwise velocity T_v (experiments E1, $U_\infty = 4.5\ \mathrm{m\,s^{-1}}$).

where the ratio T_v/T_u (or T_v/T_w) reaches a value of 5. Computing the integral timescales for experiments E2 leads again to the same conclusion. In this situation T_v/T_u is even larger than for pure wind waves. Since the usual Taylor hypothesis is valid in the low-frequency range, integral timescales can be transformed directly into integral lengthscales. The fact that $T_v \gg T_u$ or T_w indicates that, while most of the energy of u' and w' (in the low-frequency range) is contained in structures of similar extent along the streamwise direction, v' is mainly associated with elongated structures. The most plausible picture of the turbulent field in the region influenced by the waves is thus that most of the low-frequency turbulent motions associated with u' and w' belong to eddies of spanwise axis but streamwise vortices also exist and contain most of the energy of the spanwise motions. It may be worth mentioning that specific streaky structures known as Langmuir cells can develop below surface waves propagating on a shear current (see Leibovich 1983 for a review). The connection between such cells and the behaviour displayed by v' deserves investigation in the future.

5. Dynamical properties of the turbulence below periodic waves

As described in §2.2, the total velocity fluctuations recorded below mechanically generated waves were first filtered with a phase-averaging algorithm, and the short-wave contribution was processed with the aid of the LST. This approach gives access to the time history of the turbulent signals $u'(t)$ and $w'(t)$, providing a unique opportunity to shed light on modulation properties and small-scale structure of the turbulent motion for the E2 experimental series.

5.1. *Statistical properties and modulation*

Figure 10 shows a typical phase variation (just below the wave troughs) of the periodic contribution to the diagonal elements $\langle r_{11}\rangle = \langle u'^2\rangle$ and $\langle r_{33}\rangle = \langle w'^2\rangle$ of the phase-averaged Reynolds stress tensor. These quantities are clearly modulated at the frequency of the periodic waves. Below the troughs $\langle r_{11}\rangle$ and $\langle r_{33}\rangle$ are nearly twice their mean values. This modulation is present in all measurements located above $z = -75$ mm, i.e. $|kz| \leqslant 0.3$. A different illustration of the modulation property is

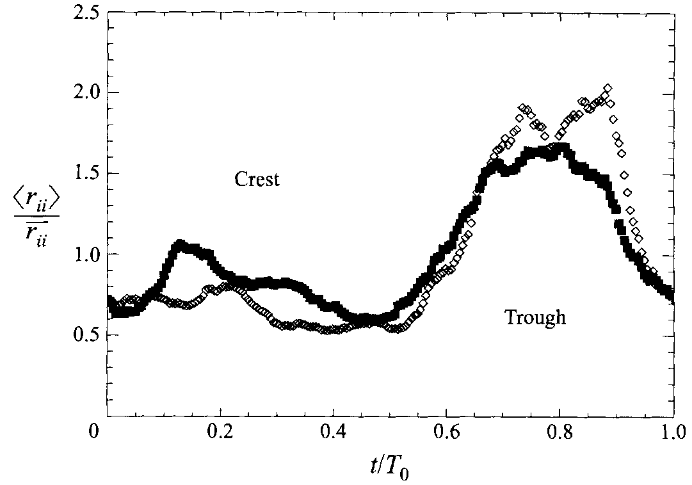

FIGURE 10. Modulation of the diagonal components of the Reynolds stress tensor along the wave phase; ■, streamwise component $\langle r_{11}\rangle$; ◇, vertical component $\langle r_{33}\rangle$ (experiments E2, $U_\infty = 4.5\ \mathrm{m\,s^{-1}}$).

depicted in figure 11(*a*) where vertical profiles of $\langle r_{11}\rangle$ averaged over 1/8 of period at the wave trough and the wave crest are presented (the properties described below also hold for $\langle r_{33}\rangle$). It appears that just underneath the surface the averages of $\langle r_{11}\rangle$ are 2.5 times larger under the troughs than under the crests. The modulation depicted by figure 11(*a*) can be interpreted in two different ways. First it can be the result of a maximum of turbulence production below the troughs. More likely, it can result from the kinematics of the surface, i.e. from the fact that at a given position z the non-dimensional distance $(z+\eta)/\delta$ from the instantaneous surface level is obviously much smaller below the troughs than below the crests. Jiang & Street (1991) have already shown that fixed-frame measurements can be very misleading. They compared two sets of results obtained in fixed-frame and wave-following experiments. While both sets looked very different when plotted in their own coordinate system, they were in close agreement after a suitable geometrical transformation. Below the trough level this kinematic distortion can be checked easily, starting from figure 11(*a*). For that purpose the vertical profiles below the trough and the crest are replotted in figure 11(*b*) versus $(z+\eta)/\delta$. The profiles seem now to collapse on a single curve, meaning that most of the modulation displayed by figure 11(*a*) comes in fact from the kinematics of the surface. Nevertheless, even compared in the same frame, our results for the modulation of the Reynolds stresses are very different from those of Jiang & Street (1991). The reason for this is that these authors only used a phase-averaging method for extracting the orbital motion from the total velocity fluctuation. Thus their 'turbulent' motions included ripple-induced motions. In contrast, in the present work, these motions are extracted by the LST; hence our results should more clearly reveal the turbulent field. Although our measurements are confined to the region below the troughs, several remarks can yet be made. It is clear that the modulation is not purely sinusoidal. This is to be contrasted with the observations made for oscillating pipe flows where the turbulence was found to respond linearly to periodic oscillations (Tardu, Binder & Blackwelder 1987). This departure from the sinusoidal behaviour has important implications for turbulence modelling since it suggests that a simple eddy viscosity model will fail to predict the turbulence below

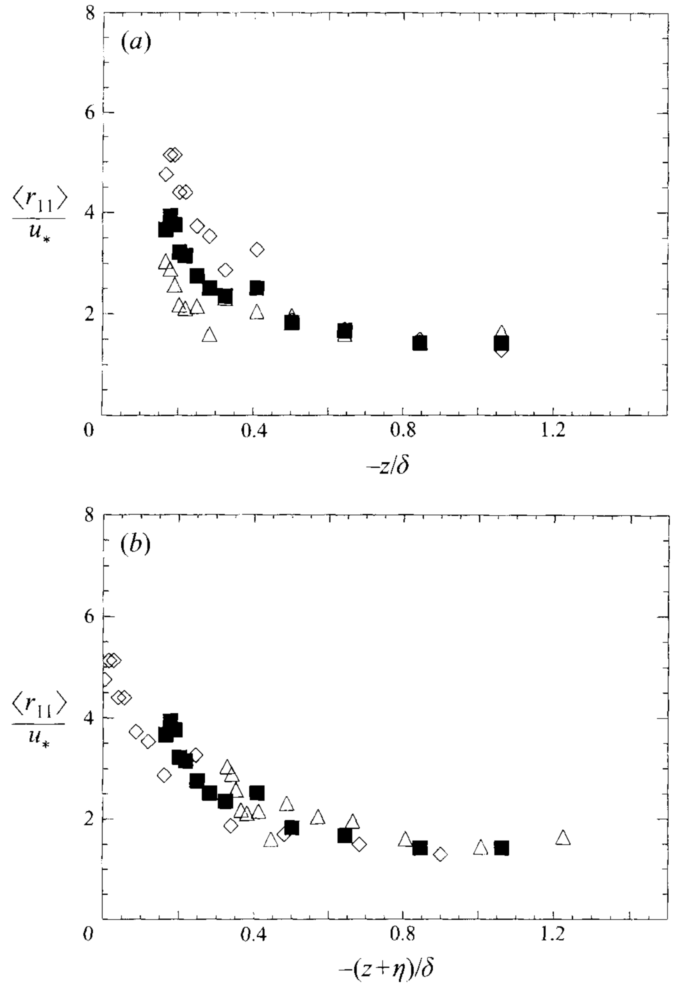

FIGURE 11. Diagonal component $\langle r_{11}\rangle$ of the Reynolds stress tensor phase averaged at: △, the wave crest; ◇, the wave trough; ■, mean value. (*a*) Plotted versus $-z/\delta$, (*b*) plotted versus $-(z+\eta)/\delta$.

the waves. As discussed by Belcher *et al.* (1994), in the immediate vicinity of the surface there should exist an inner region of thickness l_w, with

$$l_w = \frac{2\kappa}{ak}\left(\frac{\rho_a}{\rho_w}\right)^{1/2} u_{*a} \approx \frac{2\kappa}{k}\frac{u_*}{c}, \tag{5.1}$$

in which turbulence is essentially in equilibrium and thus can be described through an eddy viscosity concept. In the present study we have $6\,\text{mm} \leqslant l_w \leqslant 10\,\text{mm}$. Outside this thin layer turbulence is subject to rapid distortion by the orbital motion. Consequently, except for the measuring points very close to the trough, when these troughs are passing over the probe volume measure, our fixed-frame measurements are always in the outer region of the flow. Thus the highly non-sinusoidal behaviour displayed by the results shown in figure 10 is consistent with Belcher *et al.*'s (1994) arguments.

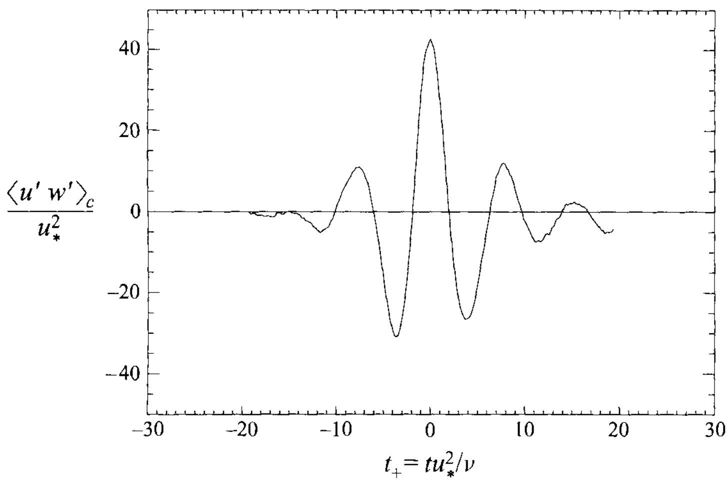

FIGURE 12. Conditional average $\langle u'w'\rangle_c$ of the phase-averaged Reynolds stress $\langle u'w'\rangle$ during bursting events.

5.2. *Bursting events*

Given that the large scales of the turbulent motion are strongly modulated by the waves it is of interest to study bursting near the surface, as well as its possible modulation by the waves. To our knowledge very few attempts have been made up to now to identify coherent structures below waves and it seems that no decisive information concerning the specific role of the waves can be drawn from them for the following reasons. Yoshikawa *et al.* (1988) applied conditional techniques to the total fluctuating motion (below wind waves), making it difficult to draw unambiguous conclusions about the structure of the turbulent field. The experiments reported by Komori, Nagaosa & Murakami (1993) consisted of generating tiny wind waves in a short and narrow channel making it unlikely that these waves might modify significantly the bursting phenomena in the water. In our investigation the bursting events were studied using classical conditional-averaging techniques, namely, (i) VITA; (ii) U-level and; (iii) Quadrant (Blackwelder & Kaplan 1976; Alfredsson & Johansson 1984; Bogard & Tiedermann 1986). The usual detection criteria of these methods were modified so as to take into account the modulation of turbulence by the waves (Tardu *et al.* 1987).

As in usual boundary layers downward bursts are the most frequent events detected by all three methods. The detected events are associated with very high instantaneous shear stresses as shown on figure 12 where the conditional average of a shear stress arising from the VITA technique has been plotted. In this example the conditional average of $\langle u'w'\rangle$ is up to 30 times its mean value, indicating very intense and intermittent momentum transfer from the surface region toward the core of the flow.

These conditional-averaging methods can be used to explore the effect of waves on bursting through comparison to typical ejection frequencies reported for wall boundary layers. As an example, in the following we analyse the results obtained at the intermediate wind speed 4.5 m s^{-1}. When scaled with the viscous timescale $t_* = \nu/u_*^2$, the mean ejection frequency $\overline{f_{e+}}$ near the free surface is found to be $\overline{f_{e+}} = 0.025$ with the VITA technique, $\overline{f_{e+}} = 0.028$ with the U-level technique and $\overline{f_{e+}} = 0.051$ with the quadrant method. The quadrant technique gives a surprisingly high result whereas the VITA and U-level results are in good agreement. The

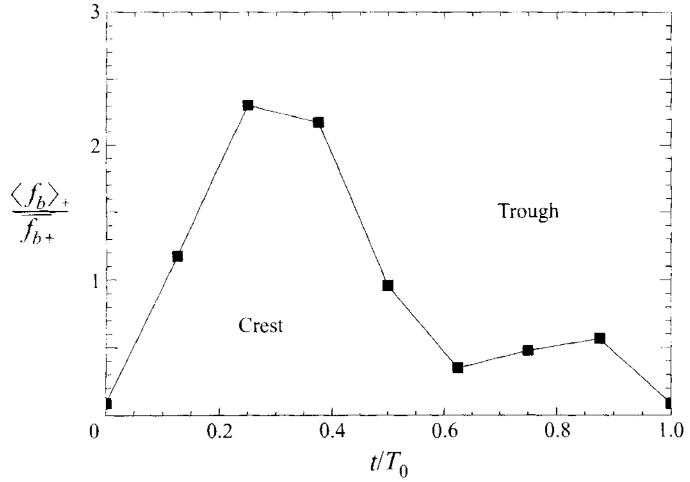

FIGURE 13. Modulation of the bursting frequency along the wave phase (experiments E2, $U_\infty = 4.5$ m s^{-1}, $z = -30.5$ mm).

quadrant method probably suffers contamination due to the uncertainty on $\langle u'w' \rangle$, owing to the phase-averaging method used to obtain this quantity. Nevertheless, even considering only the two lowest values, the mean ejection frequencies are twice as much as those observed in steady or unsteady wall boundary layers, where $\overline{f_{e+}} = 0.012$ (Bogard & Coughran 1987). This result indicates that the waves strongly promote the ejection phenomena, i.e. that the mechanism governing the ejections is not controlled only by the mean shear rate.

It is well-known that conditional averaging techniques applied to fixed-frame single-point measurements identify bursting events at different stages of their existence. Standard techniques allow to identify the individual ejections within each burst (Houdeville & Corjon 1988) and to compute a mean bursting frequency $\overline{f_b}$. The final result is $\overline{f_{b+}} = 0.014$. This is again about twice as large as observed in steady or unsteady wall bounded flows, where $\overline{f_{b+}} = 0.0062$ (Bogard & Coughran 1987). Not only is the mean bursting frequency affected but its phase average $\langle f_b \rangle_+$ is also strongly modulated along the wave phase. Figure 13 shows a typical phase dependence of the ratio $\langle f_b \rangle_+ / \overline{f_{b+}}$. To compute $\langle f_b \rangle_+$ the wave phase was sliced into 8 equal intervals and each detected burst counted in the appropriate phase interval. Figure 13 shows that the bursting frequency $\langle f_b \rangle_+$ is dramatically increased at the wave crest, a result that confirms the observations made by Komori *et al.* (1993) using high-speed video pictures. The same holds for the ejection frequency (not shown here). If the time needed to advect the structures down to the measurement point can be neglected, these results suggest that the turbulent activity is mainly concentrated below wave crests. Owing to the geometrical distortion caused by fixed-frame measurements and discussed before, such a conclusion does not conflict with the distributions found for $\langle r_{11} \rangle$ and $\langle r_{33} \rangle$. Physical processes capable of explaining such a high turbulence generation near the crest are discussed in the last section.

6. Wave–turbulence interactions

All the results reported above demonstrate that turbulence under surface waves can be substantially different from that of 'normal' wall flows. In contrast, the experiments reported in I did not show such behaviour. In this last section we identify a criterion for the occurrence of wave–turbulence interactions and try to pinpoint the basic mechanisms of such interactions.

6.1. *An energetic criterion for the occurrence of effective wave–turbulence interactions*

Wave–turbulence interactions can be considered effective when the turbulent kinetic energy is significantly enhanced with respect to usual levels encountered in wall-bounded shear flows. On the basis of this definition, we are in a position to identify a non-dimensional parameter that governs such interactions. It was shown in I that when the wind blows over the water surface, the wave-induced motion does not remain potential. Theoretically all the correlations between the potential ($\tilde{\boldsymbol{v}}_P$) and the rotational ($\tilde{\boldsymbol{v}}_R$) contributions of the orbital motion scale with a dimensionless parameter $R^2 = [ak(c - \bar{U})/u_*]^2$ which is nothing other than the ratio between the wave kinetic energy at the surface and the wind shear. To check whether wave–turbulence interactions also scale with R^2 we analyse the laboratory measurements reported here, those discussed in I and in CS, and the field measurements of Kitaigorodskii *et al.* (1983) on Lake Ontario.

In the CS wind-wave experiments and in I, R^2 lies in the range 25–85. In these experiments no significant wave–turbulence interactions were observed. On the other hand, the present study involves R^2 of order 200 for experiments E1, and of order 600 in experiments E2; likewise the CS mechanical-wave experiments correspond to a value of R^2 of order 300. In all these three latter cases significant wave-turbulence interactions were observed. The most striking results are of course those of Kitaigorodskii *et al.* (1983) which involved R^2 of order 1200. In figure 14 we have plotted as a function of R the maximum values of $(\overline{u'^2})^{1/2}/u_*$ reported in each experiment considered above. Wind-wave data (closed symbols) seem to fit a power law, determined through a least-squares interpolation to be $0.2R^{1.2}$. In contrast, mechanical-wave data (open symbols) seem to be saturated around $(\overline{u'^2})^{1/2}/u_* \approx 4.0$. However the mechanical waves used by CS and those used in the present experiments have nearly the same characteristics (only the energy carried by the ripples is significantly different). Thus there are probably too few data involving mechanical waves to conclude whether differences exist between wave–turbulence interactions that depend on the nature of the waves (i.e. random or periodic). In contrast the results for wind waves reported in figure 14 show a clear tendency: the larger the ratio R, the higher the turbulence level. In other terms for a given amount of surface shear the turbulence level increases with the energy available in the wave field.

6.2. *Efficient turbulent timescales*

To identify which eddies are the most likely to transform wave energy into turbulence we shall compare, following Kitaigorodskii & Lumley (1983), the turbulent timescales with the wave period T_0 (or dominant wave period for random waves). 'Fast' turbulent fluctuations are those with timescales significantly less than the wave period, $\tau_t \ll T_0$. Such small-scale turbulence exists at any depth but should dominate the energy-containing scales only in a very thin layer of water with maximum thickness l_w of order 10 mm in laboratory experiments (cf. §5.1). Thus, except in this layer, its role in extracting energy from the wave field is presumably small (Phillips 1961). 'Slow' turbulent fluctuations are those with timescales much larger than the wave period, $\tau_t \gg T_0$. Such turbulent fluctuations are frozen on the timescale of the wave motion so that we cannot expect them to be able to interact with the waves. Thus, only

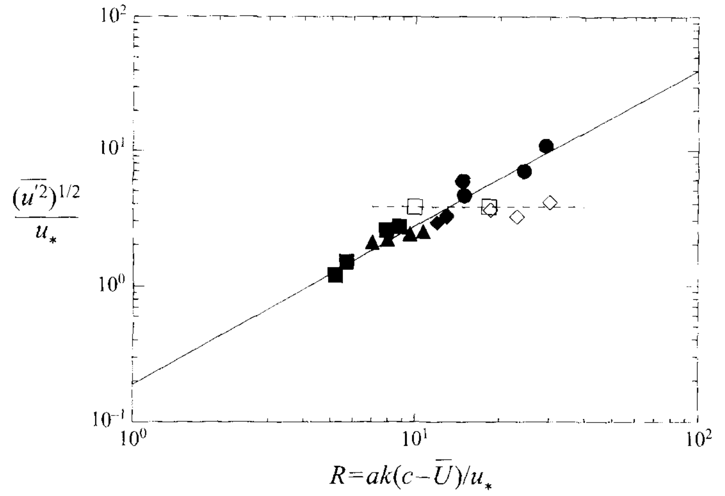

FIGURE 14. Maximum value of the streamwise r.m.s. turbulent velocity near the surface in the following experiments: ■, I; ◆, this study, experiments E1 (wind waves); ▲, CS, wind waves; ●, Kitaigorodskii *et al.* 1983; ◇, this study, experiments E2 (mechanical waves); □, CS, mechanical waves; ——, $(\overline{u'^2})^{1/2}/u_* = 0.188R^{1.2}$.

Experiment	Wave period T_0	Kolmogorov timescale	Taylor microscale	Integral timescale
E1	0.5	0.06	?	10
E2	1.0	0.04	0.2	20
I	0.3	0.10	?	5

TABLE 3. Timescales (in s) for different experimental conditions.

turbulence with intermediate timescales, i.e. turbulence with timescales of the same order as the wave motion, $\tau_t \approx T_0$, is likely to be efficient for wave–turbulence interactions.

Different timescales are reported in table 3, namely the wave period T_0 (or the dominant wave period of random waves), the Kolmogorov timescale of the dissipative range, the integral timescale and the Taylor microscale when available. These timescale estimates come from present experiments E1, E2, and I at similar wind conditions around 6.0 m s^{-1}; the depth was a few centimetres below the mean water level. In short-fetch wind-wave experiments (I), the Kolmogorov timescale was of the order of the dominant wave period (0.3 s for the former and 0.1 s for the latter). This means that turbulent motions with timescales around T_0 in I were very near the active dissipative range. Consequently, eddies that would have been most efficient at extracting wave energy were immediately damped by the dissipation. This is probably the reason why we noticed no significant increase of the turbulent kinetic energy in I. In contrast, experiments E1 and E2 exhibit a Kolmogorov timescale one order of magnitude smaller than the wave period. In these experiments efficient eddies can develop over a wide frequency range, thus allowing wave–turbulence interactions to take place. Note that these timescale arguments may be easily connected to the values of R discussed above, and in fact to the wave age.

6.3. *Turbulent kinetic energy budgets*

A natural way to identify the physical processes which contribute to increase the turbulence level is to study the turbulent kinetic energy balance. In the case of a periodic orbital motion superimposed on a mean flow this equation was first derived by Reynolds & Hussain (1972). Its derivation for random waves is more difficult since the final result depends on the assumptions made to separate the fluctuating motion into orbital and turbulent contributions. However it was pointed out in I that using the TDM for that purpose leaves this equation essentially unchanged with respect to the case of periodic waves. Assuming the mean flow is one-dimensional the general form of the turbulent kinetic energy balance in the high-Reynolds-number limit reads

$$\frac{\bar{\mathrm{D}}}{\mathrm{D}t}\overline{k_t} = \underbrace{-\overline{u'w'}\frac{\partial \bar{U}}{\partial z}}_{\text{(i)}} \underbrace{-\overline{\widetilde{v_i'v_j'}\frac{\partial \tilde{v}_i}{\partial x_j}}}_{\text{(ii)}} - \epsilon_T - \frac{\partial}{\partial z}\left[\overline{\frac{p'}{\rho}w'} + \left(\overline{k_t w'} + \overline{\tilde{k}_t \tilde{w}}\right)\right], \qquad (6.1)$$

where k_t is the instantaneous turbulent kinetic energy and $\bar{\mathrm{D}}/\mathrm{D}t = \partial/\partial t + \bar{U}\partial/\partial x$. Among the terms of the right-hand side three contributions can be deduced from the measurements, namely the production by the mean shear, $-\overline{u'w'}\,\partial\bar{U}/\partial z$, i.e. term (i) in (6.1), the downward transport of the turbulence by itself $-\partial/\partial z(\overline{k_t w'})$ and the dissipation rate ϵ_T. Turbulence diffusion by the orbital motion, i.e. the last term in (6.1), can also be computed in mechanical wave experiments. In contrast neither the pressure-diffusion contribution $-\partial/\partial z(\overline{p'w'/\rho})$ nor the direct production by the orbital motion, term (ii) in (6.1), can be evaluated. As CS previously made clear, there is too much uncertainty on the phase angles of $\widetilde{v_i'v_j'}$ to estimate properly term (ii). This comes from the fact that our measurements are fixed-frame which causes the phase angles to be locked to the phase angle of the troughs. The other expected significant terms were computed as follows. The dissipation rate was estimated using the model of Lumley & Terray (1983) as explained in §3. The turbulent transport term was computed through a least-squares polynomial fit of the $\overline{k_t w'}$ vertical profiles. Figure 15 shows typical vertical profiles of the three contributions. Even though there is a noticeable uncertainty in each term (mainly in the dissipation), the balance is roughly satisfied by the three contributions together. Moreover it is clear from this figure that production by the mean shear is almost negligible in comparison to the other terms. This is true for all wind conditions and for all types of waves. In other words, below the wave troughs the turbulent kinetic energy budget consists roughly of a balance between turbulent diffusion and dissipation. Obviously such a balance cannot explain the very high turbulence level revealed by our measurements. Since the conditional signal processing discussed in §5.1 shows unambigously that the turbulent field and its dynamic characteristics are highly modulated by the waves we have to conclude that intense wave–turbulence interactions leading to turbulence production occur in the wavy region above the troughs.

6.4. *The physical mechanisms of wave–turbulence interactions*

Even though our measurements do not provide us with sufficient information to unambiguously explain the basis for wave–turbulence interactions in this particular flow, it seems worthwhile to consider some physical processes that might be important. We will distinguish between 'indirect' mechanisms involving coupling between the mean current, the orbital motion and the turbulence and 'direct' mechanisms involving only turbulence generation by the orbital motion.

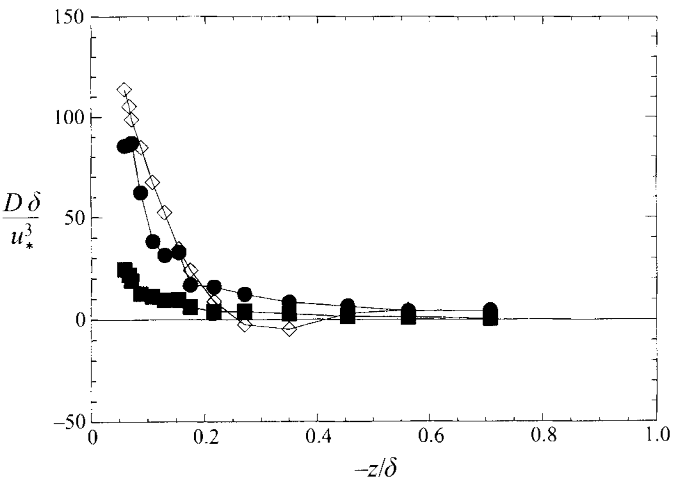

FIGURE 15. Main terms of the turbulent kinetic energy budget: ■, production $D = -\overline{u'w'}\,\partial\bar{U}/\partial z$; ◇, diffusion $D = \partial(\overline{k_t w'})/\partial z$; ●, dissipation $D = \epsilon_T$ (experiments E1, $U_\infty = 5.9\ \mathrm{m\,s^{-1}}$).

Discussing indirect coupling mechanisms requires considering the kinetic energy balances of the mean flow and the orbital motion. Using notation similar to that of (6.1) they can be written as (Reynolds & Hussain 1972)

$$\frac{\bar{\mathrm{D}}}{\mathrm{D}t}\bar{\tilde{k}} = -\overline{\tilde{u}\tilde{w}}\frac{\partial \bar{U}}{\partial z} - \overline{\widetilde{v_i'v_j'}\frac{\partial \tilde{v}_i}{\partial x_j}} - \epsilon_W - \frac{\partial}{\partial z}\left[\overline{\frac{\tilde{p}}{\rho}\tilde{w}} + \left(\overline{\widetilde{v_i'w'}\tilde{v}_i} + \overline{\tfrac{1}{2}\tilde{v}_i\tilde{v}_i\tilde{w}}\right)\right], \tag{6.2a}$$

$$\frac{\bar{\mathrm{D}}}{\mathrm{D}t}\bar{K} = \overline{\tilde{u}\tilde{w}}\frac{\partial \bar{U}}{\partial z} + \overline{u'w'}\frac{\partial \bar{U}}{\partial z} - \epsilon_M - \bar{U}\frac{\partial}{\partial x}\left(\frac{\bar{P}}{\rho}\right) - \frac{\partial}{\partial z}\left(\overline{u'w'}\bar{U}\right), \tag{6.2b}$$

where $\bar{K}$ is the kinetic energy of the mean flow, and $\tilde{k}$ the instantaneous kinetic energy of the orbital motion. From these equations it is clear that as soon as a significant wave-induced shear stress $-\overline{\tilde{u}\tilde{w}}$ exists (i.e. the wave-induced motion does not remain truly irrotational) energy exchanges occur between the mean current and the wave-induced motion. Then (6.2) implies modifications of the vertical distribution of the turbulent shear stress $-\overline{u'w'}$ which in turn can change the usual production term in (6.1). For example in their mechanical wave experiments CS measured negative wave-induced shear stresses $-\overline{\tilde{u}\tilde{w}}$ which means that the mean motion was drawing energy from the wave field. Apparently the 'excess' mean kinetic energy was redistributed to the turbulent motion through the classical positive production term $-\overline{u'w'}\,\partial\bar{U}/\partial z$.

Using an eddy viscosity relation between the turbulent shear stress and the mean shear, Magnaudet & Masbernat (1990) derived the new Reynolds stress distribution resulting from the rotational behaviour of the wave motion and explained quantitatively the increase of the turbulence level found by CS. However there are indications that this mechanism is not general. The recent analysis of Belcher *et al.* (1994) as well as the form of the modulation of the Reynolds stress tensor observed in the present experiments (see §4) suggest that the eddy-viscosity assumption is highly questionable when the turbulence is distorted by surface waves. Moreover it is easy to show that the present results cannot be explained by this interaction mechanism. As reported in §3, strong wave-induced shear stresses $-\overline{\tilde{u}\tilde{w}}$ existed in our experiments for all wave types. Amongst the present experiments and those reported in I, we found positive wave-related shear stresses in 9 out of 11 configurations. This means that the wave field was most often gaining some energy from the mean current, in contrast with the findings of CS. If the proposed mechanism held this would imply an energy transfer from the turbulence to the mean flow whereas our results reveal that turbulence can reach high levels even when $-\tilde{u}\tilde{w}$ is large and positive. Therefore this indirect mechanism is not supported by our data and cannot be considered as general.

The most obvious candidate for enhancing the turbulent energy level then becomes the direct production by the wave-induced motion, namely term (ii) in (6.1). Note first that this would be a consequence of the wave-dominated dynamics suggested by our analysis of the f^{-3} decay found in the turbulent spectra. Term (ii) in (6.1) stems directly from the term $\tilde{v}'_j \partial \tilde{v}_i / \partial x_j$ in the momentum balance. Thus if term (ii) dominates (6.1), $\tilde{v}'_j \partial \tilde{v}_i / \partial x_j$ dominates the momentum balance of the turbulent fluctuations which implies that v'_i is governed by the characteristic time t_W defined in (4.2) or (4.4). It is clear, as pointed out by Kitaigorodskii & Lumley (1983), that this term ought to be negligible when $\tilde{\boldsymbol{v}}$ satisfies the linear potential theory of gravity waves. In contrast, it may get important either when the rotational wave-induced contribution $\tilde{\boldsymbol{v}}_R$ is significant and posseses strong vertical gradients or when the wave-induced potential motion $\tilde{\boldsymbol{v}}_P$ exhibits significant departures from Stokes' solution.

The former case can occur in various situations. For example the corresponding term played a central role in the experiments of Rashidi, Hestroni & Banerjee (1992) who studied free-surface channel flows forced by long waves generated mechanically. They analysed bursting events coming from the bottom boundary layer and observed that the ejection frequency was substantially increased by surface waves. The consequence was an increase of the turbulence level with respect to the reference flow. Visualization and analysis of the wave-induced vorticity field revealed that strong negative vorticity occurred below wave crests whereas positive vorticity was found below the troughs. Since substantial wave-related Reynolds stresses $\widetilde{\boldsymbol{v}'\boldsymbol{v}'}$ associated with ejections were identified in the measurements it is highly probable that the excess of turbulence was due to the extra production involving these stresses and $\tilde{\boldsymbol{v}}_R$ gradients.

The latter case, i.e. significant production by the term (ii) in (6.1) associated with $\tilde{\boldsymbol{v}}_P$, occurs in plunging breakers but such large-scale breaking was obviously not present in our experiments. In contrast, small-scale breaking was clearly present in some of the experiments: small whitecaps were evident at the crests of the periodic waves in experiments E2, especially at the highest wind speeds. This breaking mechanism has been investigated by Phillips & Banner (1974) who showed how the tangential orbital velocity increases below the crest in the surface sublayer, due to the presence of near-surface vorticity; an increase that becomes dramatic when the wave slope goes beyond 0.2. Thus, vorticity existing at the surface (because of the wind stress) combined with the orbital motion gives rise to a mechanism capable of producing strong rotational contributions $\tilde{\boldsymbol{v}}_R$ below the wave crests. Another mechanism that can generate intense vorticity in the same region has been investigated by Longuet-Higgins (1992). He examined vorticity production by parasitic capillary ripples that ride in front of the crest of short gravity waves as confirmed by the optical analysis of Ebuchi *et al.* (1987). It is well known that curvature at a free surface forces vorticity generation. This mechanism is particularly intense with capillaries, owing to their high curvature and wavenumber. Integrating the effect of a single capillary along the whole crest region of the gravity wave, Longuet-Higgins (1992) showed that this 'wave-induced' vorticity can be sufficiently intense to generate a vortex travelling below the crest of the gravity wave. Both mechanisms suggest that vorticity generation processes specifically connected with the dynamics of the wave field are likely to act below the crest. It is highly tempting to connect these mechanisms with the most striking result discussed in §5.2, namely the prominent enhancement of the bursting frequency observed below the crest. Owing to our fixed-frame system, the bursts detected below the crest region are far from the real surface, typically several hundreds of ν/u_*. We cannot specify the location where these bursts begin to grow, owing to the intrinsic limitation of our measurement system. However it seems reasonable to assume that they are generated near the surface. If this is right, their presence and their intensity at such large distances from their origin implies that they are the result of some very intense generation process. Both mechanisms discussed above would appear to be ideal candidates. Unfortunately, measurements in the wavy region above the troughs being missing, it does not seem possible yet to confirm their role in turbulence production.

7. Conclusion

We have reported in this work the main results of an experimental study of the turbulent flow below surface waves sheared by the wind. This study has been carried out in a large wind-water tunnel where the waves induce very energetic orbital motions, compared to those used in previous laboratory experiments. Both wind-generated and mechanical waves have been considered. Depending on the type of wave, suitable separation methods have been used to extract the turbulent motion from the total fluctuating motion. Among the results revealed by these experiments the following ones appear to be the most significant:

(*a*) Turbulence reaches levels far above those observed near a solid wall submitted to the same stress. The increase of the level of turbulence can reach one order of magnitude with the most energetic (i.e. mechanical) waves used here. Estimates of the dissipation rate confirm this tendency and ensure that this trend is not the consequence of inaccurate separation of the fluctuating motions.

(*b*) The turbulent spectra exhibit a clear f^{-3} subrange beyond the frequency of the dominant wave. Possible alterations of the slopes of the frequency spectra have been examined but do not seem capable of explaining this result. In contrast, the enhancement found in the turbulence level suggests that the turbulent field is forced by the orbital motion. The result of such forcing is to impose a constant timescale t_W related to the wave strain onto a certain range of turbulent eddies which implies the f^{-3} behaviour. This assumption has been checked by estimating t_W and computing a factor which must be constant if the assumption is verified. The results strongly support this assumption and give a value $C = 0.2$ for the constant.

(*c*) The structure of the turbulent field below the waves is different from that found near a wall. For mechanical waves, through use of phase-averaging we have found that turbulence can be modulated by the wave-induced motion, not only at large but also at small scales, such that the entire range of motions is affected.

(*d*) Conditional sampling techniques have been used to study the statistics of bursting events. Under the present conditions we find that the average bursting frequency is nearly twice that observed in usual boundary layers. Moreover study of the distribution of bursting events along the wave phase shows that the probability of bursting reaches a pronounced maximum below wave crests.

(*e*) The most significant terms of the turbulent kinetic energy balance have been computed. It appears that below the trough level this balance is dominated by dissipation and turbulent transport. Among other things, this balance is not able to explain the energy level of the turbulence field.

Taken in their entirety, our results suggest that the key to the observed behaviour lies in a direct interaction between the wave-induced motion and the turbulence. Among the possible mechanisms for such an interaction, those which are responsible for vorticity generation near the crest of the dominant wave (i.e. micro-breaking and capillary ripples) are the most natural candidates and need specific investigations.

This research was partly supported by the French PAMOS Program under Grants 91/ATP/631 and 92N50/0268. Many people have contributed to this work at various stages and it is a pleasure to thank them all. We are particularly indebted to H. Poujol for his technical assistance all along the preparation and the realization of the experiments and to G. Caulliez for her help and advice during the measurements. Many thanks are due to M. A. Donelan for providing the code used for the Linear Superposition Technique and to S. G. Monismith for stimulating discussions and helpful comments during the completion of this paper.

REFERENCES

AGRAWAL, Y. C., TERRAY, E. A., DONELAN, M. A., HWANG, P. A., WILLIAMS, A. J., DRENNAN, W. M., KAHMA, K. K. & KITAIGORODSKII, S. A. 1992 Enhanced dissipation of kinetic energy beneath surface waves. *Nature* **359**, 219–220.

ALFREDSSON, P. H. & JOHANSSON, A. V. 1984 On the detection of turbulence-generating events. *J. Fluid Mech.* **139**, 325–345.

BANNER, M. L. & PEREGRINE, D. H. 1993 Wave breaking in deep water. *Ann. Rev. Fluid Mech.* **25**, 373–397.

BELCHER, S. E. & HUNT, J. C. R. 1993 Turbulent shear flow over slowly moving waves. *J. Fluid Mech.* **251**, 109–148.

BELCHER, S. E., HARRIS, J. A. & STREET, R. L. 1994 Linear dynamics of wind waves in coupled turbulent air-water flow. Part 1. Theory. *J. Fluid Mech.* **271**, 119–151.

BELCHER, S. E., NEWLEY, T. M. J. & HUNT, J. C. R. 1993 The drag on an undulated surface induced by the flow of a turbulent boundary layer. *J. Fluid Mech.* **249**, 557–596.

BENILOV, A. YU., KOUZNETZOV, O. A. & PANIN, G. N. 1974 On the analysis of wind wave induced disturbances in the atmospheric turbulent surface layer. *Boundary-Layer Met.* **6**, 269–285.

BLACKWELDER, A. F. & KAPLAN, R. E. 1976 On the bursting phenomenon near the wall in turbulent shear flows. *J. Fluid Mech.* **76**, 89–112.

BOGARD, D. G. & COUGHRAN, M. T. 1987 Bursts and ejections in a LEBU-modified boundary layer. In *6th Symp. on Turbulent Shear Flows, Toulouse.*

BOGARD, D. G. & TIEDERMANN, W. G. 1986 Burst detection with a single-point velocity measurement. *J. Fluid Mech.* **162**, 389–413.

BUCKLES, J., HANRATTY, T. J. & ADRIAN, R. J. 1984 Turbulent flow over large-amplitude wavy surfaces. *J. Fluid Mech.* **140**, 27–44.

CHEUNG, T. K. & STREET, R. L. 1988 Turbulent layers in the water at an air-water interface. *J. Fluid Mech.* **194**, 133–151 (referred to herein as CS).

COANTIC, M., RAMAMONJIARISOA, A., MESTAYER, P., RESCH, F. & FAVRE, A. 1981 Wind-water tunnel simulation of small-scale ocean-atmosphere interactions. *J. Geophys. Res.* **86**, C7, 6607–6626.

DILLON, T. M., RICHMAN, J. G., HANSEN, C. G. & PEARSON, M. D. 1981 Near-surface measurements in a lake. *Nature* **290**, 390–392.

DONELAN, M. A. 1978 Whitecaps and momentum transfer. In *Turbulent Fluxes through the Sea Surface. Wave dynamics and Prediction* (ed. A. J. Favre & K. Hasselmann). Plenum.

DONELAN, M. A., ANCTIL, F. & DOERING, J. C. 1992 A simple method for calculating the velocity field beneath irregular waves. *Coastal Engng*, **16**, 399–424.

EBUCHI, N., KAWAMURA, H. & TOBA, Y. 1987 Fine structure of laboratory wind-wave surfaces studied using an optical method. *Boundary-Layer Met.* **39**, 133–151.

GARGETT, A. E. 1989 Ocean turbulence. *Ann. Rev. Fluid Mech.* **21**, 419–451.

HOUDEVILLE, R. & CORJON, A. 1988 Phénomène de Bursting dans une couche limite pulsée de plaque plane. *Rapport ONERA RSF OA* 69/2259. CER, Toulouse.

HSU, C.-T., HSU, E.-Y. & STREET, R. L. 1981 On the structure of turbulent flow over a progressive water wave: theory and experiment in a transformed, wave-following coordinate system. *J. Fluid Mech.* **105**, 87–117.

JIANG, J. S. & STREET, R. L. 1991 Modulated flows beneath wind-ruffled, mechanically generated water waves. *J. Geophys. Res.* **96**, C2, 2711–2721.

JIANG, J. S., STREET, R. L. & KLOTZ, S. P. 1990 A study of wave-turbulence interaction by use of a nonlinear water wave decomposition technique. *J. Geophys. Res.* **95**, C9, 16037–16054.

JONES, I. S. F. 1985 Turbulence below wind waves. In *The Ocean Surface* (ed. Y. Toba & H. Mitsuyasu). Reidel.

KITAIGORODSKII, S. A. K., DONELAN, M. A., LUMLEY, J. L. & TERRAY, E. A. 1983 Wave-turbulence interactions in the upper ocean. Part II: Statistical characteristics of wave and turbulent components of the random velocity field in the marine surface layer. *J. Phys. Oceanogr.* **13**, 1988–1999.

KITAIGORODSKII, S. A. K. & LUMLEY, J. L. 1983 Wave-turbulence interactions in the upper ocean. Part I: The energy balance of the interacting fields of surface wind waves and wind-induced three-dimensional turbulence. *J. Phys. Oceanogr.* **13**, 1977–1987.

KLEBANOFF, P. S. 1955 Characteristics of turbulence in a boundary layer flow with zero pressure gradient. *NACA Rep.* 1247.

KOMORI, S., NAGAOSA, R. & MURAKAMI, Y. 1993 Turbulence structure and mass transfer across a sheared air-water interface in wind-driven turbulence. *J. Fluid Mech.* **249**, 161–183.

LAKE, B. M. & YUEN, H. C. 1978 A new model for nonlinear wind waves. Part 1, Physical model and experimental evidence. *J. Fluid Mech.* **88**, 33–62.

LEIBOVICH, S. 1983 The form and dynamics of Langmuir circulations. *Ann. Rev. Fluid Mech.* **15**, 391–427.

LEMMIN, U., SCOTT, J. T. & CZAPSKI, U. H. 1974 The development from two-dimensional to three-dimensional turbulence generated by breaking waves. *J. Geophys. Res.* **79**, 3442–3448.

LIN, J. T. & GAD-EL-HAK, M. 1984 Turbulent current measurements in a wind-wave tank. *J. Geophys. Res.* **89**, C1, 627–636.

LONGUET-HIGGINS, M. S. 1963 The generation of capillary waves by steep gravity waves. *J. Fluid Mech.* **16**, 138–159.

LONGUET-HIGGINS, M. S. 1992 Capillary rollers and bores. *J. Fluid Mech.* **240**, 659–679.

LUMLEY, J. L. & TERRAY, E. A. 1983 Kinematics of turbulence convected by a random wave field. *J. Phys. Oceanogr.* **13**, 2000–2007.

MAGNAUDET, J. & MASBERNAT, L. 1990 Interactions des vagues de vent avec le courant moyen et la turbulence. *C.R. Acad. Sci. Paris* II **311**, 1461–1466.

MAGNAUDET, J. & THAIS, L. 1995 Orbital rotational motion and turbulence below laboratory wind water waves. *J. Geophys. Res.* **100**, C1, 757–771 (referred to herein as I).

MONISMITH, S. G., MAGNAUDET, J., NEPF, H., THAIS, L., & COWEN, E. A. 1996 Mean flows under surface gravity waves. To be submitted to *J. Fluid Mech.*

NEPF, H. M., COWEN, E. A., KIMMEL, S. J. & MONISMITH, S. G. 1995 Langmuir vortices beneath breaking waves. *J. Geophys. Res.* **100**, C8 16211–16222.

PEDLOSKY, J. 1987 *Geophysical Fluid Dynamics*. Springer.

PHILLIPS, O. M. 1961 A note on the turbulence generated by gravity waves. *J. Geophys. Res.*, **66**, 2889–2893.

PHILLIPS, O. M. 1977 *The Dynamics of the Upper Ocean*. Cambridge University Press.

PHILLIPS, O. M. 1981 Dispersion of short wavelets in the presence of a dominant long wave. *J. Fluid Mech.* **107**, 465–485.

PHILLIPS, O. M. & BANNER, M. L. 1974 Wave breaking in the presence of wind drift and swell. *J. Fluid Mech.* **66**, 625–640.

RAMAMONJIARISOA, A. 1974 Contribution à l'étude de la structure statistique et des mécanismes de génération des vagues de vent. Thèse d'Etat, Université de Provence, Aix-Marseille I.

RASHIDI, M., HESTRONI, G. & BANERJEE, S. 1992 Wave-induced interaction in free-surface channel flows. *Phys. Fluids* A **4**, 2227–2238.

REVAULT D'ALLONNES, M. 1982 Une hypothèse sur la structure de la turbulence induite dans l'eau par les vagues fortement cambrées. *C.R. Acad. Sci.* **295**, 201–203.

REYNOLDS, W. C. & HUSSAIN, A. K. M. F. 1972 The mechanics of an organized wave in turbulent shear flow. Part 3. Theoretical model and comparisons with experiments. *J. Fluid Mech.* **54**, 263–288.

SOMMERIA, J. & MOREAU, R. 1982 Why, how, and when, MHD turbulence becomes two-dimensional. *J. Fluid Mech.* **118**, 507–518.

TARDU, F. S., BINDER, G. & BLACKWELDER, R. 1987 Modulation of bursting by periodic oscillations imposed on channel flow. In *6th Symp. on Turbulent Shear Flows, Toulouse.*

TENNEKES, H. & LUMLEY, J. L. 1972 *A First Course in Turbulence.* MIT Press.

TERRAY, E. A. & BLIVEN, L. F. 1985 The vertical structure of turbulence beneath gently breaking waves. In *The Ocean Surface* (ed. Y. Toba & H. Mitsuyasu). Reidel.

TERRAY, E. A., DONELAN, M. A., AGRAWAL, Y. C., DRENNAN, W. M., KAHMA, K. K., WILLIAMS, A. J., HWANG, P. A., & KITAIGORODSKII, S. A. 1996 Estimates of kinetic energy dissipation under breaking waves. *J. Phys. Oceanogr.* **26**, 792–807.

THAIS, L. 1994 Contribution à l'étude du mouvement turbulent sous des vagues de surface cisaillées par le vent. Thèse Inst. Nat. Polytech. Toulouse.

THAIS, L. & MAGNAUDET, J. 1995 A triple decomposition of the fluctuating motion below laboratory wind water waves. *J. Geophys. Res.* **100**, C1, 741–755 (referred to herein as II).

VEYNANTE, D. & CANDEL, S. 1988 Application of nonlinear spectral analysis and signal reconstruction to laser Doppler velocimetry. *Exps. Fluids* **6**, 534–540.

YOSHIKAWA, I., KAWAMURA, H., OKUDA, K. & TOBA, Y. 1988 Turbulent structure in water under laboratory wind waves. *J. Ocean. Soc. Japan* **44**, 143–156.